

12-2008

MODELING, ANALYSIS AND CONTROL OF FLEXIBLE SOLID-STATE HYSTERETIC ACTUATORS

Kushan Vora

Clemson University, kvora@clemson.edu

Follow this and additional works at: https://tigerprints.clemson.edu/all_theses



Part of the [Engineering Mechanics Commons](#)

Recommended Citation

Vora, Kushan, "MODELING, ANALYSIS AND CONTROL OF FLEXIBLE SOLID-STATE HYSTERETIC ACTUATORS" (2008).
All Theses. 497.

https://tigerprints.clemson.edu/all_theses/497

This Thesis is brought to you for free and open access by the Theses at TigerPrints. It has been accepted for inclusion in All Theses by an authorized administrator of TigerPrints. For more information, please contact kokeefe@clemson.edu.

MODELING, ANALYSIS AND CONTROL OF FLEXIBLE SOLID-STATE
HYSTERETIC ACTUATORS

A Thesis
Presented to
the Graduate School of
Clemson University

In Partial Fulfillment
of the Requirements for the Degree
Master of Science
Mechanical Engineering

by
Kushan Vora
December 2008

Accepted by:
Dr. Nader Jalili, Committee Chair
Dr. Darren Dawson
Dr. Mohammed Daqaq

ABSTRACT

A distributed parameters modeling and control framework for flexible solid-state hysteretic actuator is presented in this work. For the simplicity of analysis, the actuator dynamic behavior is decoupled and treated separately from the hysteresis nonlinearity. To include the effects of widely-used flexural mechanisms, a mass-spring-damper boundary condition is considered for system. Moreover, the effect of electromechanical actuation is included as a concentrate force at the boundary. The problem is then divided into two parts: first part deals with free motion analysis of system in order to obtain eigenvalues and eigenfunctions using the expansion theorem and a standard eigenvalue problem procedure. The effects of different boundary mass and spring values on the natural frequencies and mode shapes are demonstrated, which indicate their significant contribution to system performance.

In the second part, forced motion analysis of system and its state-space representation are presented. A frequency based control strategy utilizing widely used Lyapunov theorem is designed to obtain an accurate control over the actuator motion. A robust variable structure control is incorporated into the developed controller for compensation of ever-present plant structural uncertainties. A full order state feedback observer is designed to accurately mimic the states of an unobservable plant. An optimization algorithm is developed to compute the optimal observer gain matrix. Various frequency tracking simulations are performed using feedback controller-observer model to observe the effect of modes deficiency on the tracking frequency bandwidth of the controller.

Finally, for the accurate prediction of nonlinear multi-loop hysteresis effect, a major source of inaccuracies at quasi-static frequency, a recently developed hysteresis model based on three hysteric properties of piezoelectric material namely *targeting of turning points, curve*

alignment and the *wiping-out effect* is used. Initially, the hysteresis nonlinearity is decoupled from the looping effect and modeled separately using an exponential function. The obtained exponential function is then utilized in a nonlinear mapping procedure, where it is mapped between consequent turning points recorded in model memory unit. This mapping also uses four constant shaping parameters - two for the ascending and two for the descending hysteresis trajectories. A proportional integral (PI) controller is used for the compensation of hysteresis nonlinearity. Performance of PI controller is validated using several numerical simulations. Finally, the method of combining robust feedback control strategy with the feedforward hysteresis compensation technique is presented to accomplish the precise control over actuator motion.

DEDICATION

To my parents and my friend Saeid Bashash

ACKNOWLEDGMENTS

I am thankful to my academic adviser, Dr. Nader Jalili for his guidance and support during my master's studies. I am grateful to the fellow student and friend Dr. Saeid Bashash, without his guidance and support this work would not possible. I also want to thank my advisory committee, Dr. Daren Dawson and Dr. Mohammed Daqaq for their helpful suggestions. Continuous support from Dr. Dapino and Ohio State University is also appreciated.

TABLE OF CONTENTS

ABSTRACT.....	i
DEDICATION.....	iv
ACKNOWLEDGMENTS	v
LIST OF FIGURES	viii
LIST OF TABLES.....	xi
1. INTRODUCTION	1
1.1 Research Background and Literature Review	1
1.2 Research Motivation	5
1.3 Thesis Contributions	6
1.4 Thesis Overview.....	6
2. DISTRIBUTED PARAMETERS MODELING OF ROD-LIKE SOLID STATE ACTUATORS.....	9
2.1 System Configurations and Modeling.....	9
2.2 System Governing Equations	10
2.3 Free Motion Analysis	12
2.4 Forced Motion Analysis	14
2.5 Numerical Simulations and Results	17
2.5.1 Effect of end mass and spring on natural frequencies of the actuator.....	17
2.5.2 Effect of end mass and spring on the mode shapes of the actuator.....	18
3. TRACKING CONTROL OF ROD-LIKE SOLID STATE ACTUATORS.....	21
3.1 State-space Controller Development.....	21
3.1.1 State-space controller design.....	22
3.1.2 Numerical validation of the state-space controller	24
3.1.2.1 Effects of tracking frequency on the controller performance	26
3.1.2.2 Effect of control gains on the tracking performance	27
3.2 Observer Development.....	28
3.2.1 Observer design	29
3.2.2 Optimal selection of observer gain matrix	30

3.2.3 Numerical validation of the observer	32
3.2.3.1 Effect of gain matrix on the observer performance	32
3.3 State-Space Controller with Observer.....	34
3.3.1 Numerical validation of the assembled controller and observer	34
3.3.2 Effect of modes defeciancy on the tracking performance	37
3.3.3 Effect of controller gains on the steady state tracking error	38
3.4 Robust Control of the Galfenol Actuator	40
3.4.1 Sliding mode controller design.....	40
3.4.2 Replacement of sliding mode control by soft switching variable structure control	43
3.4.3 Numerical validation of the variable structure control	45
3.4.4 Comparison of variable structure control with the sliding mode control	46
3.4.5 Gain tuning of variable structure controller	47
4. HYSTERESIS MODELING AND COMPANSATION	51
4.1 Introduction	51
4.2 Experimental Setup and Results.....	52
4.3 Modeling Nonlinearities using Average Curve Model	55
4.3.1 Average Curve Model	55
4.3.2 Experimental Results and Numerical Simulations	56
4.4 Memory-based Hysteresis Modeling	57
4.4.1 Mathematical formulation	58
4.4.2 Experimental Verification	60
4.5 Proportional - Integral (PI) Hysteresis Control	63
5. CONCLUSIONS AND FUTURE WORKS	66
5.1 Conclusion.....	66
5.2 Future Works and Directions	67
APPENDIX.....	69
REFERENCES	73

LIST OF FIGURES

2.1	Schematic representation of a rod-like actuator (left) and its representative distributed-parameters model (right).....	9
2.2	Natural frequencies of first four modes versus (a) increasing values of spring stiffness ' k ' and (b) increasing values of end mass ' m '.....	17
2.3	(a) First, (b) second, (c) third and (d) fourth mode shape of actuator for four different configurations of end mass and spring (C1 — , C2 —⊕— , C3 - - - , C4 ··+··)	19
3.1	State-space controller-plant block diagram for desired trajectory tracking.....	24
3.2	Tracking control results for 1, 20, 50 and 100 kHz sinusoidal desired trajectories using the proposed state-space controller.....	26
3.3	Steady state tracking error comparison, for 1, 20, 50 and 100 kHz sinusoidal trajectories. 27	
3.4	100 kHz frequency tracking errors using three different pairs of controller	28
3.5	Results using optimization algorithm for concentrating the poles of the system at -1000, -20000 and -50000 on the real axis.	31
3.6	Observer/plant diagram for the accurate state estimation.....	32
3.7	Convergence of the observer state estimation errors to zero.	33
3.8	state estimation for three different observer gain matrices.	33
3.9	Integrated controller/observer diagram for precise plant control.	34
3.10	Tracking control results for 1, 20, 50 and 100 kHz sinusoidal reference inputs using combined controller/observer strategy.....	36
3.11	Steady state tracking error comparison for 1, 20, 50 and 100 kHz sinusoidal desired trajectories.....	36
3.12	Different approximations and tracking control results for a (a, b) 1-mode; (c, d) 2- mode; (e, f) 3-mode; (g, h) 4-mode (full) reprwsentation of the system	39
3.13	Steady-state tracking error comparisons for two different sets of controller gains for controller/observer based on two modes approximation.	39
3.14	Graphical representation of sliding mode control.....	42
3.15	Graphical representation of variable structure control.....	44

3.16	50 kHz sinusoidal desired input tracking using variable structure control, (a) control input applied to the plant, and (b) tracking result	46
3.17	50 kHz sinusoidal reference input tracking using sliding mode control; (a) control input applied to the plant, (b) tracking result, and (c) phase portrait comparison of variable structure control with hard switching sliding mode control	47
3.18	Effect of robustness condition on the variable structure control; (a) phase portrait when robustness condition is satisfied, and (b) phase portrait when robustness condition is not satisfied	48
3.19	Effect of ε on the soft switching variable structure control	49
3.20	Effect of σ on the soft switching variable structure control	49
4.1	Experimental setup for a Galfenol-driven micro-positioning actuator.	52
4.2	Nonlinear hysteretic response of Galfenol actuator: (a) Input current profile, (b) actuator displacement, and (c) butterfly-like hysteresis loops.....	54
4.3	Response of average curve model: (a) the average curve between the ascending and descending hysteresis curves, and (b) comparison with the actuator response.	56
4.4	(a) Separation of nonlinearity from the hysteresis loops, and (b) typical multi-segment internal path.	60
4.5	Performance of the memory based hysteresis model: (a) model vs. experimental time responses, and (b) model hysteresis response.....	61
4.6	Minor hysteresis loops of (a) experimental and (b) memory-based model response.	61
4.7	Error comparison of the average curve model and the memory-based hysteresis.....	62
4.8	Simulation of hysteresis model: (a) input profile, (b) butterfly hysteresis response, (c) left minor loops, and (d) right minor loops.	63
4.9	Hysteresis control using Proportional Integral control strategy	64
4.10	Hysteresis control results: (a) and (b) for 500Hz sinusoidal desired input, (c) and (d) for 1000Hz sinusoidal desired input.....	64
5.1	Combined hysteresis and actuator dynamics control scheme using combination of state-space and PI controller.....	68
5.2	Combined hysteresis and actuator dynamics control scheme using combination of state-space and inverse hysteresis controllers	69

5.3	Hysteresis prediction using inverse hysteresis model.....	69
-----	---	----

LIST OF TABLES

2.1 Actuator parameters used in the simulations for calculating natural frequencies of the actuator.....	17
2.2 Actuator parameters used for numerical simulations to calculate mode shapes.....	18
3.1 Steady state error at different tracking frequencies	27
4.1 Comparison of the error values for the average curve model and the memory-based hysteresis model.....	63
4.2 Proportional and Integral gain values for 500 and 1000Hz sinusoidal desired input	65

CHAPTER 1

INTRODUCTION

1.1 Research Background and Literature Review

Until the past few years, most of the technological developments were linked to the invention of materials. Materials used in most of these applications were either passive or not functional, as they do not sense or respond in a predictable manner to the change in the environment. The recent technological innovations in material science engineering have resulted in materials that can change their physical properties in a predictable or controllable manner by application of external stimuli are referred as smart materials ^{1,2} . The utilization of smart materials in today's world ranges from very small NEMS (Nano Electro-Mechanical Systems) and MEMS (Micro Electro-Mechanical Systems) applications ^{3,4} to large aerospace applications ^{5,6} . Piezoelectric materials, ferromagnetic materials and shape memory alloys are some of the examples of smart materials.

Piezoceramics are one of the most widely used smart materials due their sub-micro meter resolution with large bandwidth and few gigahertzes operating frequency. Piezoelectric actuators made up of lead zirconate titanate (PZT) are used in various fields. However, the fatigue and aging phenomenon associated with piezoelectric actuators limits their usage ^{7,8} . Due to these limitations, ferromagnetic actuators made up of Galfenol and Terfenol-D are becoming increasingly popular. Terfenol-D, an alloy of terbium, dysprosium and iron metals developed by U.S. Naval ordnance laboratory has very high magnetostriction property at room temperature, when compared to other ferromagnetic materials ⁹ . It generates 2-5 times greater strains than

traditional piezoceramics and 20 times more than any other ferromagnetic material ⁹ . The applications of Terfenol-D are restricted due to brittleness as well as lower tensile and sheer strength at room temperature.

Galfenol, a new Fe-Ga alloy was developed in 1998 by magnetic materials group at NSWC-CD (Naval Surface Warfare Center) ⁹ . “Galfenol possesses key additional advantages; that is, unlike most active materials, Galfenol is malleable and machinable ¹⁰, and can be safely operated under simultaneous tension, compression, bending and shock loads. As a consequence of the unique combination of metallurgical and mechanical properties of Galfenol, this material can enable smart load-carrying Galfenol devices and structures with innovative 3-D manufactured by welding, extrusion, rolling, deposition, or machining. Furthermore, the unprecedented control of anisotropies through manufacturing and post-processing methods made possible with Galfenol ¹¹ can lead to innovative devices with fully coupled 3-D functionality¹².”^{*} Due to micrometer resolution, fast frequency response and capability to withstand high stresses, Galfenol actuators are rapidly replacing other ferromagnetic and piezoelectric actuators used for micro-positioning, active vibration damping and sensing applications in the field of aerospace engineering ¹³ , medical technology, atomic force microscopy ^{14,15} , microscale manufacturing, etc. However, these immerging applications in various fields require precise control of the Galfenol actuator.

The control performance of Galfenol actuators is limited by two main factors: (i) material-level nonlinearities such as hysteresis and creep, and (ii) dynamical effects of system

^{*}Bashash S., Vora K., Jalili N., Evans P. G., and Dapino M., “Memory-based hysteresis compensation and nonlinear modeling of Galfenol-driven micro-positioning actuators,” in *Proceedings of 1st ASME Dynamic Systems and Control Conference, October 2008, Ann Arbor, MI.*

inertia, flexibility and damping ¹⁶ . Many methods have been developed to deal with hysteresis nonlinearity ¹⁷⁻²¹ . Some of these works have considered hysteresis effect and dynamic behavior simultaneously by introducing the rate-dependent hysteresis modeling ¹⁹, whereas majority of them have filtered the hysteresis nonlinearity using various approaches and controlled the dynamic behavior of the actuator, independently from the hysteresis nonlinearity. However, in order to achieve precise control over the actuator dynamics, an accurate modeling framework is very essential. For the simplicity in analysis and control strategy development, many works have considered the lumped-parameters representation of the actuator ^{20,21} . Although such a lumped-parameter model is valid below the first natural frequency of system, it starts to deviate if the operational frequency passes over the first mode. Therefore, a distributed-parameters representation is preferred in higher operational frequencies. The, rod-like Galfenol actuators have distributed-parameters dynamics; that is, their equations of motion are described by partial differential equations with appropriate boundary conditions ^{22,23} . The approximate methods such as finite element or finite difference schemes have been utilized to solve these partial differential equations of motion.

Apart from these dynamic effects caused by internal and external forces, most smart actuators also suffer from the material level hysteresis nonlinearities. Several hysteresis frameworks are developed to predict these hysteresis nonlinearities. Most of these frameworks are either based on constitutive approach ^{24,25} or based on phenomenological approach ^{26,27} . The constitutive hysteresis models use the physics behind the hysteresis phenomenon whereas the phenomenological models utilize the mathematical structure for prediction of hysteresis²⁸. The most widely used *Preisach* model ²⁹ which is based on phenomenological approach, has very accurate hysteresis prediction capability without providing any physical insight of the hysteresis

phenomenon²⁸. However, the constitutive models based on nonlinear mapping technique and utilizing intelligent properties of hysteresis phenomenon developed by *Bashas et al.*³⁰ have almost the same hysteresis prediction accuracy with much lesser mathematical parameters.

Along with actuator characterization, much research work is emphasized in achieving the precise control of the distributed-parameters actuator model as well. Control schemes for these systems are mainly categorized into two control methods: (i) feedforward control and (ii) feedback control. However, for many applications, feedback control schemes are combined with the feedforward methods to achieve the high frequency tracking control of these actuators.

Various inverse hysteresis modeling frameworks are developed for the feedforward compensation of hysteresis nonlinearity. Most of these models are built based on two fundamental methods: (i) inverse hysteresis curve identification using different numerical techniques³¹, and (ii) analytical approach that computes the inverse hysteresis curve using identified hysteresis model^{28,32}. The performance of these feedforward hysteresis compensation strategies highly depends on the hysteresis prediction accuracy of forward as well as inverse hysteresis models.

Different feedback control strategies such as Proportional Integral Derivative (PID) control³³, robust adaptive control³⁴ and feedforward neural network controller with a fixed-gain feedback control³⁵ are used in order to achieve the control over dynamic behavior of the actuators. The PID controller is utilized to control the lumped-parameters system models. Due to its inability to place more than two poles of the system at their desired locations, PID control fails to control the higher order (higher than second order) systems for high frequency applications. On the other hand, Lyapunov based control strategies are utilized for controlling

higher order distributed-parameters systems. Robust and adaptive features are incorporated into these controllers for compensation of structural uncertainties as well as ever present unmodeled dynamics. The neural networks based feedback controllers are also known for the precise micro-positioning and control applications. The online feedforward neural network based control strategy is developed that utilizes a fixed gain feedback control to train neural network controller such that it forces the output of feedback controller to be zero. In this way neural network controller learns the inverse dynamics of the system and forces it to follow the desired trajectory³⁵.

1.2 Research Motivation

Although several modeling and control frameworks have been proposed by the researchers for characterization and precision control of the smart actuators, most of them have modeled these smart actuators as lumped or distributed-parameters beams and not as rods. The sensitivity of the techniques used for control of these actuators become much more significant, when they are used for micro-positioning applications, and any further improvement in the accuracy is highly desirable. Also, most previous works have rarely given any emphasis on the development of control strategies for the unobservable plant models. Furthermore, there is real need for hysteresis predictive model for accurate hysteresis characterization. The presently used hysteresis characterization techniques like *Preisach* model are much more complicated and need much more computations due to large amount of mathematical parameters. The work presented here is aimed at modeling of smart actuators as a distributed-parameters rod and controlling them using precise and less complicated combined feedforward and feedback robust control strategies.

The hysteresis model developed here needs much lesser mathematical computations with approximately the same or better amount of modeling accuracy than conventionally used models.

1.3 Thesis Contributions

A distributed-parameters modeling and robust control framework for flexible rod-like solid-state Galfenol actuator is presented here. The effects of flexure mechanisms are incorporated into the model using spring-mass-damper boundary conditions. The electromechanical actuation is included as a concentrated force at the boundary. The free as well as force motion analyses are performed to understand the dynamic behaviour of the actuator. A unique frequency based robust variable structure control strategy is built using Lyapunov theory. A full order state feedback observer is designed to mimic the states of the unobservable plant. An optimization algorithm is then developed to compute the optimal observer gain matrix. Several frequency tracking simulations are performed to observe the effect of modes deficiency on tracking frequency bandwidth of the controller. Recently developed piezoelectric hysteresis model utilizing memory based nonlinear mapping technique is used for the hysteresis prediction of Galfenol actuator. The accurate hysteresis predictive ability with much less mathematical computations compared to other hysteresis models is verified using simulations. A proportional integral (PI) control strategy is utilized for the compensation of hysteresis nonlinearity. Finally, numerical simulations using PI controller are carried out to validate its hysteresis compensation performance for 500 and 1000Hz sinusoidal desired input.

1.4 Thesis Overview

The development and analysis of distributed-parameters model of rod-like solid-state actuator is presented in the immediately following chapter. For the simplicity of analysis,

dynamic behavior of the actuator is decoupled from the hysteresis nonlinearity and treated separately. Effects of widely-used flexural mechanisms are incorporated into the actuator using a mass-spring-damper boundary condition. Moreover, the effect of electromechanical actuation is included as a concentrate force at the boundary. To observe the contributions of boundary mass and spring on the actuator dynamic properties, the effects of different end mass and spring values on the natural frequencies and mode shapes are demonstrated using simulations.

Chapter 3 represents the control strategy for distributed-parameters actuator model developed in Chapter 2. A frequency based robust variable structure controller utilizing Lyapunov theory, a full order state feedback observer for replication of the states of unobservable plant and an optimization algorithm for computation of optimal observer gain matrix are designed in this chapter. Various high frequency tracking simulations are performed to validate the performance of the controller-observer model.

A feedforward hysteresis compensation technique is presented in Chapter 4. For the accurate hysteresis prediction, the hysteresis nonlinearity is decoupled from the looping effect and modelled utilizing an exponential function. This function is then used in a hysteresis predictive model utilizing memory based mapping technique. The three intelligent hysteresis properties, *target of turning points*, *curve alignment* and *wiping-out effect*, are incorporated in the model for further hysteresis prediction accuracy. A proportional integral control is used for control of hysteresis nonlinearity. Hysteresis control results of for the 500 as well as 1000Hz desired sinusoidal input are presented.

Finally the conclusion and future directions for present work are described in Chapter 5. Developed robust variable structure control (for the control of actuator dynamics) and

proportional control (for the hysteresis compensation) can be combined the in future to achieve the precise positioning control over the actuator motion. The inverse hysteresis model utilizing the similar mapping technique as forward model can be designed and utilized in future for the hysteresis compensation. Also, a hysteresis minor loops shape changing mechanism can be incorporated in the hysteresis modeling framework for achieving the better accuracy in hysteresis minor loop prediction.

CHAPTER 2

DISTRIBUTED PARAMETERS MODELING OF ROD-LIKE SOLID STATE ACTUATORS[†]

2.1 System Configurations and Modeling

The importance of state-space modeling for the actuator is very important in the availability of standard controllers for obtaining the desired motion of actuator. The work presented here is aimed at (i) obtaining the modal characteristics including natural frequencies and mode shapes of the free vibrating actuator, (ii) observing the effect of the end mass ' m ' and spring ' k ' on the natural frequencies and mode shapes of the actuator, and (iii) obtaining state-space representation by carrying out the forced motion analysis of system.

Figure 1 depicts the schematic configuration as well as representative model of a typical rod-like actuator. The actuator has a mass per unit length ρ , stiffness E , viscous damping coefficient B , length L , and cross-sectional area A which is modeled as a distributed-parameters rod subjected to a compound boundary condition of a mass m , damper C and spring k as shown in Figure 1. Moreover, the effective excitation force $f(t)$, which comes from a distributed internal stress, can be applied at the boundary as a concentrate actuation force.

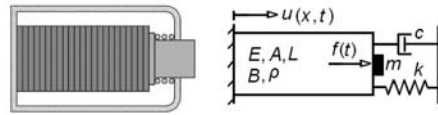


Figure 2.1 Schematic representation of a rod-like actuator (left) and its representative distributed-parameters model (right)

[†]The content of this chapter may have come directly or indirectly from our joint publication: [Vora K., Bashash S., and Jalili N., "Distributed parameters modeling of rod-like solid-state actuators," in *Proceedings of 1st ASME Dynamic Systems and Control Conference, October 2008, Ann Arbor, MI.*]

2.2 System Governing Equations

The governing equation for the longitudinal (axial) vibrations of the actuator subjected to axial force $f(t)$ at the end is derived using the extended Hamiltonian principal given by:

$$\int_{t_1}^{t_2} (\delta(T - V) + \delta W_{ext}) dt = 0 \quad (2.1)$$

where T , V and W_{ext} are respectively the kinetic energy, potential Energy and the external work of the rod in the presence of longitudinal time varying force $f(t)$. The longitudinal displacement $u(x, t)$ is assumed to be varying over the entire length of the actuator.

The kinetic energy of the actuator having length L , fixed mass per unit density ρ and the end mass m can be given by:

$$T = \frac{1}{2} \int_0^L \rho \left(\frac{\partial u(x, t)}{\partial t} \right)^2 dx + \frac{1}{2} m \left(\frac{\partial u(L, t)}{\partial t} \right)^2 \quad (2.2)$$

The potential energy of the actuator with fixed Young's modules of elasticity E and cross-sectional area A is given by:

$$V = \frac{1}{2} \int_0^L EA \left(\frac{\partial u(x, t)}{\partial x} \right)^2 dx + \frac{1}{2} k u^2(L, t) \quad (2.3)$$

The external work done by excitation force $f(t)$, uniformly-distributed damping force and the damping force at the boundary is represented as:

$$\delta W_{ext} = f(t) \delta u(L, t) - \int_0^L B \left(\frac{\partial u(x, t)}{\partial t} \right) \delta u(x, t) dx - C \left(\frac{\partial u(L, t)}{\partial t} \right) \delta u(L, t) \quad (2.4)$$

Substituting the derived kinetic energy (2.2), potential energy (2.3) and variation of external work by (2.4) into Eq. (2.1), applying variational principle and by rearranging all the terms, it yields:

$$\begin{aligned} & \int_{t_1}^{t_2} \int_0^L \left\{ -\rho \left(\frac{\partial^2 u(x,t)}{\partial t^2} \right) \delta u(x,t) + EA \left(\frac{\partial^2 u(x,t)}{\partial x^2} \right) \delta u(x,t) - B \left(\frac{\partial u(x,t)}{\partial t} \right) \delta u(x,t) \right\} dx dt \\ & + \int_{t_1}^{t_2} \left\{ -m \left(\frac{\partial^2 u(L,t)}{\partial t^2} \right) \delta u(L,t) - EA \left(\frac{\partial u(L,t)}{\partial x} \right) \delta u(L,t) - C \left(\frac{\partial u(L,t)}{\partial t} \right) \delta u(L,t) \right. \\ & \left. - ku(L,t) \delta u(L,t) + f(t) \delta u(L,t) \right\} dt = 0 \end{aligned} \quad (2.5)$$

Since the integral from t_1 to t_2 must vanish, the integrant must vanish. Hence, Eq. (2.5) can be written as:

$$\begin{aligned} & \left\{ -\rho \left(\frac{\partial^2 u(x,t)}{\partial t^2} \right) + EA \left(\frac{\partial^2 u(x,t)}{\partial x^2} \right) - B \left(\frac{\partial u(x,t)}{\partial t} \right) \right\} \delta u(x,t) \\ & + \left\{ -m \left(\frac{\partial^2 u(L,t)}{\partial t^2} \right) - EA \left(\frac{\partial u(L,t)}{\partial x} \right) - C \left(\frac{\partial u(L,t)}{\partial t} \right) - ku(L,t) + f(t) \right\} \delta u(L,t) = 0 \end{aligned} \quad (2.6)$$

Since $\delta u(x,t)$ and $\delta u(L,t)$ are arbitrary variables, we have:

$$\delta u(x,t) \neq 0 \text{ and } \delta u(L,t) \neq 0 \quad (2.7)$$

Consequently, Eq. (2.6) reduced to:

$$\rho \left(\frac{\partial^2 u(x,t)}{\partial t^2} \right) - EA \left(\frac{\partial^2 u(x,t)}{\partial x^2} \right) + B \left(\frac{\partial u(x,t)}{\partial t} \right) = 0 \quad (2.8)$$

And

$$m \left(\frac{\partial^2 u(L,t)}{\partial t^2} \right) + EA \left(\frac{\partial u(L,t)}{\partial x} \right) + C \left(\frac{\partial u(L,t)}{\partial t} \right) + ku(L,t) = f(t) \quad (2.9)$$

Eqs. (2.8) and (2.9) represent the equation of motion and the boundary condition for the system, respectively.

2.3 Free Motion Analysis

Modal characterization of the system is performed using a standard procedure for the free and undamped equations. The equation of motion is modified to:

$$\rho \left(\frac{\partial^2 u(x,t)}{\partial t^2} \right) = EA \left(\frac{\partial^2 u(x,t)}{\partial x^2} \right) \quad (2.10)$$

Let's assume that solution of Eq. (2.10) is separable in time and space domains. By applying separation of variable, the longitudinal displacement function of rod can be written as:

$$u(x,t) = \phi_r(x) q_r(t) \quad (2.11)$$

where $\phi_r(x)$ is the spatial mode shape function and $q_r(t)$ represents the generalized time dependant coordinate.

Substituting Eq. (2.11) into Eq. (2.10) yields:

$$\left(\frac{\ddot{q}_r(t)}{q_r(t)} \right) = \left(\frac{EA}{\rho} \right) \frac{\phi_r''(x)}{\phi_r(x)} = -\omega_r^2 \quad (2.12)$$

where ω_r is a constant parameter that represents the natural frequency for the r^{th} mode of actuator. Hence, Eq. (2.12) can be split into two time-domain and spatial equations as follows:

$$\ddot{q}_r(t) + \omega_r^2 q_r(t) = 0 \quad (2.13)$$

$$\phi_r''(x) + \beta_r^2 \phi_r(x) = 0 \quad (2.14)$$

where β_r is represented as:

$$\beta_r^2 = \frac{\rho \omega_r^2}{EA} \quad (2.15)$$

The general solution of the equation of motion in spatial domain can be written as:

$$\phi_r(x) = C_r \sin \beta_r x + D_r \cos \beta_r x \quad (2.16)$$

At the fixed end of the actuator we have $\phi_r(0) = 0$, hence $D_r = 0$. Therefore, the mode shapes of the actuator are modified to:

$$\phi_r(x) = C_r \sin \beta_r x \quad (2.17)$$

Now applying the separation of variable to the free and undamped boundary condition of the actuator yields:

$$m\phi_r(L)\ddot{q}_r(t) + EA\phi_r'(L)q_r(t) + k\phi_r(L)q_r(t) = 0 \quad (2.18)$$

By substituting Eq. (2.13) and Eq. (2.17) into Eq. (2.18) and simplifying it further, the characteristics equation is obtained as follows:

$$-\left(\frac{EA}{\rho}\right)\beta_r^2 m + EA\beta_r \cot(\beta_r L) + k = 0 \quad (2.19)$$

The numerical solution of (2.19) yields infinite solutions for β_r . Natural frequencies corresponding to each β_r can be found using Eq. (2.15).

Based on natural frequencies, the mode shapes for the r^{th} mode can be calculated as:

$$\phi_r(x) = C_r \sin\left(\sqrt{\frac{\rho}{EA}} \omega_r x\right) \quad (2.20)$$

where C_r is a mode-dependant constant and can be calculated using normalization with respect to mass (for derivation of the normalization condition, refer to appendix A) which can be given as:

$$\rho \int_0^L \phi_r(x) \phi_s(x) dx + m \phi_r(L) \phi_s(L) = \delta_{rs} \quad (2.21)$$

δ_{rs} is the knonecker delta defined as $\delta_{rs} = 1$ if $r = s$ and $\delta_{rs} = 0$ otherwise.

Substituting Eq. (2.20) into Eq. (2.21) and simplifying it, C_r can be obtained as:

$$C_r = \left[\rho \int_0^L \sin^2 \left(\omega_r \sqrt{\frac{\rho}{EA}} x \right) dx + m \sin^2 \left(\omega_r \sqrt{\frac{\rho}{EA}} L \right) \right]^{-\frac{1}{2}} \quad (2.22)$$

2.4 Forced Motion Analysis

By applying the expansion theorem to the longitudinal displacement of actuator the displacement can be written as:

$$u(x, t) = \sum_{r=1}^{\infty} \phi_r(x) q_r(t) \quad (2.23)$$

Substituting Eq. (2.23) into the partial differential equation of motion of the actuator, Eq. (2.8) is written as:

$$\sum_{r=1}^{\infty} \{ \rho \phi_r(x) \ddot{q}_r(t) - EA \phi_r''(x) q_r(t) + B \phi_r(x) \dot{q}_r(t) \} = 0 \quad (2.24)$$

Taking integral over the entire length of rod, multiplying it by $\phi_s(x)$ and applying integral by parts, Eq. (2.24) is converted to:

$$\sum_{r=1}^{\infty} \left\{ \rho \ddot{q}_r(t) \int_0^L \phi_r(x) \phi_s(x) dx - EA q_r(t) \phi'_r(L) \phi_s(L) + EA q_r(t) \int_0^L \phi_r(x) \phi_s(x) dx + B \dot{q}_r(t) \int_0^L \phi_r(x) \phi_s(x) dx \right\} = 0 \quad (2.25)$$

Now substituting Eq. (2.23) into the boundary condition at $x = L$, Eq. (2.9) yields:

$$\sum_{r=1}^{\infty} \{ m \phi_r(L) \ddot{q}_r(t) + EA \phi'_r(L) q_r(t) + C \phi_r(L) \dot{q}_r(t) + k \phi_r(L) q_r(t) \} = f(t) \quad (2.26)$$

Substituting $EA \phi'_r(L) q_r(t)$ from Eq. (2.26) into Eq. (2.25) and simplifying it further one can get,

$$\sum_{r=1}^{\infty} \left\{ \left[\rho \int_0^L \phi_r(x) \phi_s(x) dx + m \phi_r(L) \phi_s(L) \right] \ddot{q}_r(t) + \left[B \int_0^L \phi_r(x) \phi_s(x) dx + C \phi_r(L) \phi_s(L) \right] \dot{q}_r(t) + \left[EA \int_0^L \phi_r(x) \phi_s(x) dx + k \phi_r(L) \phi_s(L) \right] q_r(t) \right\} = \phi_s(L) f(t) \quad (2.27)$$

Applying the orthogonality conditions with respect to mass and stiffness (refer to Appendix A for the derivations) given as:

$$\rho \int_0^L \phi_r(x) \phi_s(x) dx + m \phi_r(L) \phi_s(L) = \delta_{rs} \quad (2.28)$$

and

$$EA \int_0^L \phi'_r(x) \phi'_s(x) dx + k \phi_r(L) \phi_s(L) = \omega_r^2 \delta_{rs} \quad (2.29)$$

Eq. (2.27) is simplified to:

$$\sum_{r=1}^{\infty} \left\{ \delta_{rs} \ddot{q}_r(t) + \left[B \int_0^L \phi_r(x) \phi_s(x) dx + C \phi_r(L) \phi_s(L) \right] \dot{q}_r(t) + \omega_r^2 \delta_{rs} q_r(t) \right\} = \phi_s(L) f(t) \quad (2.30)$$

Where $r = 1, 2, \dots$

Eq. (2.30) can be recast as:

$$\ddot{q}_r(t) + \sum_{s=1}^{\infty} \{c_{rs} \dot{q}_s(t)\} + \omega_r^2 q_r(t) = f_r(t) \quad (2.31)$$

where

$$c_{rs} = B \int_0^L \phi_r(x) \phi_s(x) dx + C \phi_r(L) \phi_s(L), \quad (2.32)$$

$$f_r(t) = \phi_r(L) f(t) \quad (2.33)$$

The truncated k -mode description of Eq. (2.31) can be presented in the following matrix form:

$$\mathbf{M} \ddot{\mathbf{q}}(t) + \mathbf{C} \dot{\mathbf{q}}(t) + \mathbf{K} \mathbf{q}(t) = \mathbf{F} u \quad (2.34)$$

where

$$\mathbf{M} = [\mathbf{I}]_{k \times k}, \quad \mathbf{C} = [c_{rs}]_{k \times k}, \quad \mathbf{K} = [\omega_r^2 \delta_{rs}]_{k \times k}, \quad (2.35)$$

$$\mathbf{q} = [q_1(t), q_2(t), \dots, q_k(t)]_{k \times 1}^T \quad (2.36)$$

$$\mathbf{F} = [\phi_1(L), \phi_2(L), \dots, \phi_k(L)]_{k \times 1}^T \quad (2.37)$$

$$u = f(t) \quad (2.38)$$

The state-space representation of Eq. (2.34) is given by:

$$\dot{\mathbf{x}} = \mathbf{A} \mathbf{x} + \mathbf{B} u \quad (2.39)$$

where

$$\mathbf{A} = \begin{bmatrix} \mathbf{0} & \mathbf{I} \\ -\mathbf{M}^{-1} \mathbf{K} & -\mathbf{M}^{-1} \mathbf{C} \end{bmatrix}_{2k \times 2k}, \quad \mathbf{B} = \begin{bmatrix} \mathbf{0} \\ \mathbf{M}^{-1} \mathbf{F} \end{bmatrix}_{2k \times 1} \quad (2.40)$$

$$\mathbf{x} = \begin{Bmatrix} \mathbf{q} \\ \dot{\mathbf{q}} \end{Bmatrix}_{2k \times 1} \quad (2.41)$$

2.5 Numerical Simulations and Results

To study the effect of end mass and spring on the natural frequencies and mode shapes of the actuator, a set of numerical simulations is carried out which is presented in the following subsections.

2.5.1 Effect of end mass and spring on natural frequencies of the actuator

The first four natural frequencies of the system are plotted in Figure 2.2(a) versus different values of spring constant k , setting m to zero, and in Figure 2.2(b) versus increasing values of end mass m taking k as zero. All other parameters used for the numerical simulations are listed in Table 2.1.

Table 2.1 Actuator parameters used in the simulations for calculating natural frequencies of the actuator

ρ	d	L	E
(kg / m ³)	(m)	(m)	(Gpa)
6000	0.01	0.1	100

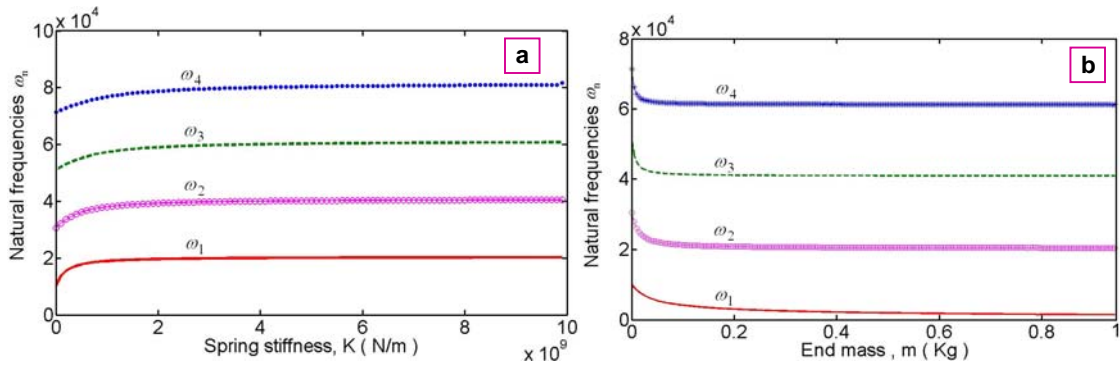






Figure 2.2 Natural frequencies of first four modes versus (a) increasing values of spring stiffness ‘ k ’ and (b) increasing values of end mass ‘ m ’.

It can be observed from the Figure 2.2 that at initial stage of the simulations, as the stiffness of the spring increases, the natural frequencies of all the actuator modes increase exponentially and eventually converge to some specific values. This happens because of the fact that rod with a large spring constant at the end behaves similar to the rod that has both its ends clamped. The similar phenomenon occurs in a reverse way with increasing values of the end mass. That is, as the value of end mass increases, natural frequencies decrease until they get saturated.

2.5.2 Effect of end mass and spring on the mode shapes of the actuator

To observe the behavior of actuator mode shapes with the change in spring stiffness and end mass of actuator, first four actuator mode shapes are plotted with four different end mass and spring stiffness configurations as: (i) zero end mass, high spring stiffness, (ii) zero end mass, zero spring stiffness, (iii) moderate end mass, moderate spring stiffness, and (iv) high end mass, high spring stiffness. Results of the simulations are depicted in Figure 2.3, with the selected parameters for the simulations listed in Table 2.2.

Table 2.2 Actuator parameters used for numerical simulations to calculate mode shapes

Configuration	m (kg)	k (N/m)	ω_1 (kHz)	ω_2 (kHz)	ω_3 (kHz)	ω_4 (kHz)
C1 	0	10^{10}	20.25	40.5	60.76	81
C2 	0	0	10.21	30.62	51.03	71.44
C3 	0.02	10^4	7.31	24.09	43.04	62.79
C4 	1	0	1.39	20.5	40.87	61.27

Other Actuator parameters:

Viscous damping coefficient: $B = 0.1 \text{ (N.sec/m}^2\text{)}$,

Discrete damping coefficient: $C = 0.05 \text{ (N.sec/m)}$,

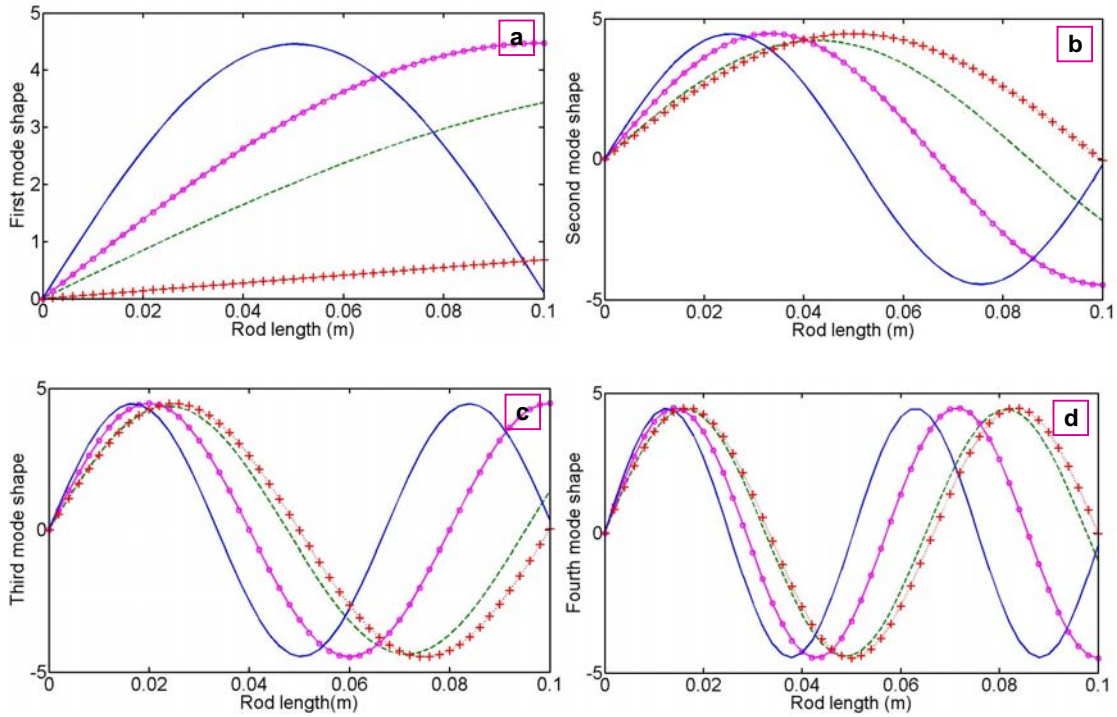


Figure 2.3 (a) First, (b) second, (c) third and (d) fourth mode shape of actuator for four different configurations of end mass and spring (C1 — , C2 —○— , C3 --- , C4 —+—)

The significant changes in all the four mode shapes are observed as we switch from one end mass and spring configuration to another. By carefully observing the mode shapes, one can see that mode shapes associated with C1 configuration (zero end mass, high spring stiffness) are similar to the mode shapes of the actuator having both ends clamped. It can be also seen from the figures that the mode shapes of C4 configuration (high end mass, zero spring stiffness) follow the mode shapes of C1 configuration with one mode shift.

distributed parameter modeling and dynamic behavior analysis of the rod-like solid-state actuator in this Chapter, the Lyapunov theorem based state-space robust control strategy utilizing variable structure control is developed in Chapter 3.

Distributed parameter modeling and dynamic behavior analysis of the rod-like solid-state actuator is performed in this Chapter. Utilizing the state-space representation of the actuator developed in Chapter 2, the frequency based robust variable structure control strategy utilizing Lyapunov theorem is developed in Chapter 3.

CHAPTER 3

TRACKING CONTROL OF ROD-LIKE SOLID STATE ACTUATORS[‡]

The frequency based feed-back control strategy utilizing Lyapunov theorem is designed in this chapter. In order to mimic the actuator states the full order state observer developed for the unobservable plant. A least square optimization algorithm is developed to compute the optimal observer gain matrix. A robust variable structure control is incorporated in to the controller design for compensation of ever-present plant structural uncertainties. The tracking simulations for various frequency sinusoidal desired inputs are carried out to validate the performance of combined controller-observer strategy to achieve the precise control over the actuator motion. Finally, the effect of mode deficiency on the tracking bandwidth of the state-space frequency based controller is shown using several numerical simulations.

3.1 State-space Controller Development

Development of a straightforward state-space controller for asymptotic output tracking control of linear systems not only can benefit the present rod-like actuator, but also can be applied to a variety of dynamic systems. In this chapter, a new form of state-space control law is proposed for output tracking control of SISO mechanical systems and applied for precision control of rod-like actuators for a high bandwidth tracking application. Moreover, the development and integration of an optimally tuned state observer is presented and discussed.

[‡]The content of this chapter may have come directly or indirectly from our joint publication: [Bashash S., Vora K., Jalili N., "Distributed-parameters modeling and control of rod-type solid-state actuators," Submitted to Journal of Vibration and Control, October 2008.]

3.1.1 State-space controller design

For actuator tip to follow the desired trajectory y_d , the tracking error is defined as:

$$e(t) = y_d(t) - y(t) \quad (3.1)$$

where $y(t)$ represents the tip displacement of the actuator. Taking the time derivative of (3.1) yields:

$$\dot{e}(t) = \dot{y}_d(t) - \dot{y}(t) = \dot{y}_d(t) - C\dot{x}(t) = \dot{y}_d(t) - CAx(t) - CBu(t) \quad (3.2)$$

It is shown below using *Example 1* that for rod-like actuators or other flexible structures (e.g. beams, plates, shells) the coefficient of $u(t)$, term CB , is always zero.

Example 1: For the truncated k -mode description of equation of motion given by given by Eq. (2.34) as below:

$$\mathbf{M}\ddot{\mathbf{q}}(t) + \mathbf{C}\dot{\mathbf{q}}(t) + \mathbf{K}\mathbf{q}(t) = \mathbf{F}u \quad (3.3)$$

For $k = 2$,

Mass matrix \mathbf{M} , damping matrix \mathbf{C} , stiffness matrix \mathbf{K} and force matrix \mathbf{F} can be given as:

$$\mathbf{M} = \begin{bmatrix} 1 & 0 \\ 0 & 1 \end{bmatrix}, \quad \mathbf{C} = \begin{bmatrix} c_{11} & c_{12} \\ c_{21} & c_{22} \end{bmatrix}, \quad \mathbf{K} = \begin{bmatrix} \omega_1^2 \delta_{11} & \omega_1^2 \delta_{12} \\ \omega_2^2 \delta_{21} & \omega_2^2 \delta_{22} \end{bmatrix} \quad \text{and} \quad \mathbf{F} = [\phi_1(L), \phi_2(L)] \quad (3.4)$$

The state-space representation of Eq. (3.3) can be given as:

$$\begin{aligned} \dot{\mathbf{x}} &= \mathbf{A}\mathbf{x} + \mathbf{B}u \\ y &= \mathbf{C}\mathbf{x} + \mathbf{D}u \end{aligned} \quad (3.5)$$

where state-space system matrices \mathbf{A} , \mathbf{B} and output displacement matrix \mathbf{C} can be given as:

$$\mathbf{A} = \begin{bmatrix} \mathbf{0} & \mathbf{I} \\ -\mathbf{M}^{-1}\mathbf{K} & -\mathbf{M}^{-1}\mathbf{C} \end{bmatrix} = \begin{bmatrix} 0 & 0 & 1 & 1 \\ 0 & 0 & 1 & 1 \\ -\omega_1^2 \delta_{11} & -\omega_1^2 \delta_{12} & -c_{11} & -c_{12} \\ -\omega_2^2 \delta_{21} & -\omega_2^2 \delta_{22} & -c_{21} & -c_{22} \end{bmatrix}, \quad (3.6)$$

$$\mathbf{B} = \begin{bmatrix} 0 \\ \mathbf{M}^{-1}\mathbf{F} \end{bmatrix} = \begin{bmatrix} 0, 0, \phi_1(L), \phi_2(L) \end{bmatrix}^T \text{ and } \mathbf{C} = [1, 1, 0, 0] \quad (3.7)$$

Product of output matrix \mathbf{C} and system matrix \mathbf{B} and can be given as:

$$\mathbf{C} \cdot \mathbf{B} = [1, 1, 0, 0] \cdot \begin{bmatrix} 0, 0, \phi_1(L), \phi_2(L) \end{bmatrix}^T = 0 \quad (3.8)$$

This implies that first order state-space controller cannot be used for tracking of desired trajectory in the form of displacement. Hence, letting $CB = 0$ and differentiating one more time from (3.1) yields:

$$\ddot{e}(t) = \ddot{y}_d(t) - CA\dot{x}(t) = \ddot{y}_d(t) - CA^2x(t) - CABu(t) \quad (3.9)$$

Similarly, it can be shown using *Example 1* that the term CAB in Eq. (3.9) cannot be zero for the flexible mechanical structures. Product of output matrix \mathbf{C} , system matrices \mathbf{A} and \mathbf{B} given by Eqs. (3.6) and (3.7) can be computed as:

$$\begin{aligned} \mathbf{C} \cdot \mathbf{A} \cdot \mathbf{B} &= [1, 1, 0, 0] \cdot \begin{bmatrix} 0 & 0 & 1 & 1 \\ 0 & 0 & 1 & 1 \\ -\omega_1^2 \delta_{11} & -\omega_1^2 \delta_{12} & -c_{11} & -c_{12} \\ -\omega_2^2 \delta_{21} & -\omega_2^2 \delta_{22} & -c_{21} & -c_{22} \end{bmatrix} \cdot \begin{bmatrix} 0, 0, \phi_1(L), \phi_2(L) \end{bmatrix}^T \\ &= 2[\phi_1(L) + \phi_2(L)] \neq 0 \end{aligned} \quad (3.10)$$

Hence, the second order state-space controller can be used to control the motion of the actuator.

Claim 3.1: For the Single-Input Single-Output (SISO) state-space system given in (2.39) which satisfies $CB = 0$ and $CAB \neq 0$, the following control law leads to asymptotic convergence of the tracking error, i.e. $e \rightarrow 0$ as $t \rightarrow \infty$.

$$u(t) = \{CAB\}^{-1} \left(\ddot{y}_d(t) - CA^2x(t) + k_1\dot{e}(t) + k_2e(t) \right); \quad k_1, k_2 > 0 \quad (3.11)$$

Proof: Substituting the control law given by Eq. (3.11) into Eq. (3.9), the second order error dynamics equation is obtained as:

$$\ddot{e}(t) + k_1\dot{e}(t) + k_2e(t) = 0 \quad (3.12)$$

As k_1 and k_2 are chosen as positive coefficients, Eq. (3.12) represents a stable second order differential equation with its roots located in the left half s-plane. This implies the asymptotic convergence of the tracking error $e(t)$ as $t \rightarrow \infty$. In the next section, the proposed control law is numerically implemented on the actuator model.

3.1.2 Numerical validation of the state-space controller

In order to validate the derived state-space control law, Simulink model of the state-space plant/controller has been developed. Since the actuator is modeled as a distributed-parameters system, any desired number of modes can be included in the model. To simulate a realistic model with high bandwidth accuracy, first four modes of the actuators are included in the model. For the precise tracking, the controller is also designed based on the first four modes of the actuator.

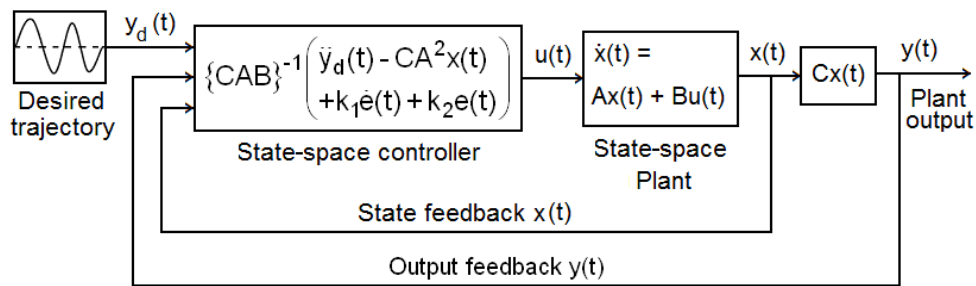
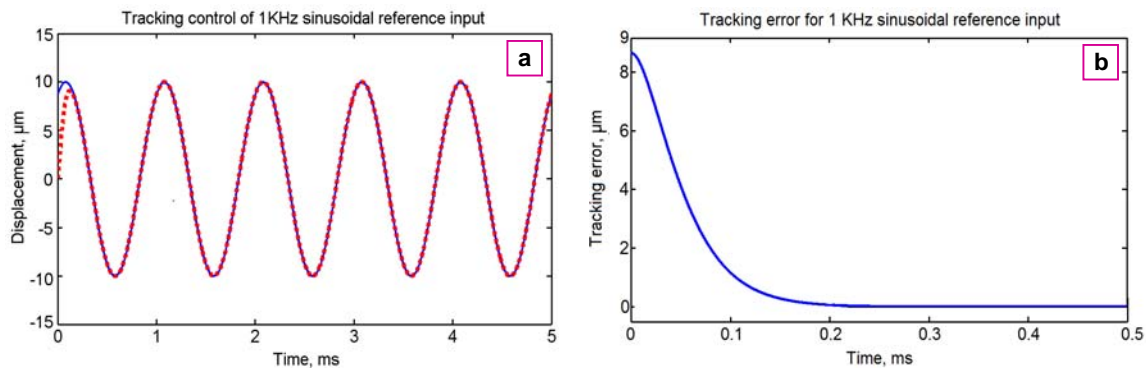


Figure 3.1 State-space controller-plant block diagram for desired trajectory tracking

Figure 3.1 depicts the block diagram of the implemented controller. As seen, for tracking the desired trajectory, controlled input is applied to the plant state-space model and the state

feedback from the plant is fed back to the controller. For accurate tracking control, selection of controller gains (k_1 and k_2) is a crucial step. In order to achieve the exponential stability with minimum oscillations of the error trajectory, the values of gains should be selected in such a way that roots of Eq. (3.12) remain on real axis, concentrated at one point, far from the imaginary axis and in the left half plane. These specifications generate a critically damped error dynamics which possesses the fastest settling time with no undesirable oscillations for a given natural frequency.

To verify the tracking performance of developed controller, a set of simulations with different tracking frequencies are carried out. The values of k_1 and k_2 and the sampling time selected for the simulations are $70000, 1.225 \times 10^9$, and 10^{-8} sec, respectively. This renders a critically error dynamics with the natural frequency of 35000 rad/sec. Figure 3.2 depicts the tracking control and the corresponding error trajectories for 1, 20, 50 and 100 kHz desired trajectories. It can be observed from the figure that by proper selection of controller gains, the tracking error associated with all the four desired trajectories converge exponentially with a settling time as low as 0.2 ms.



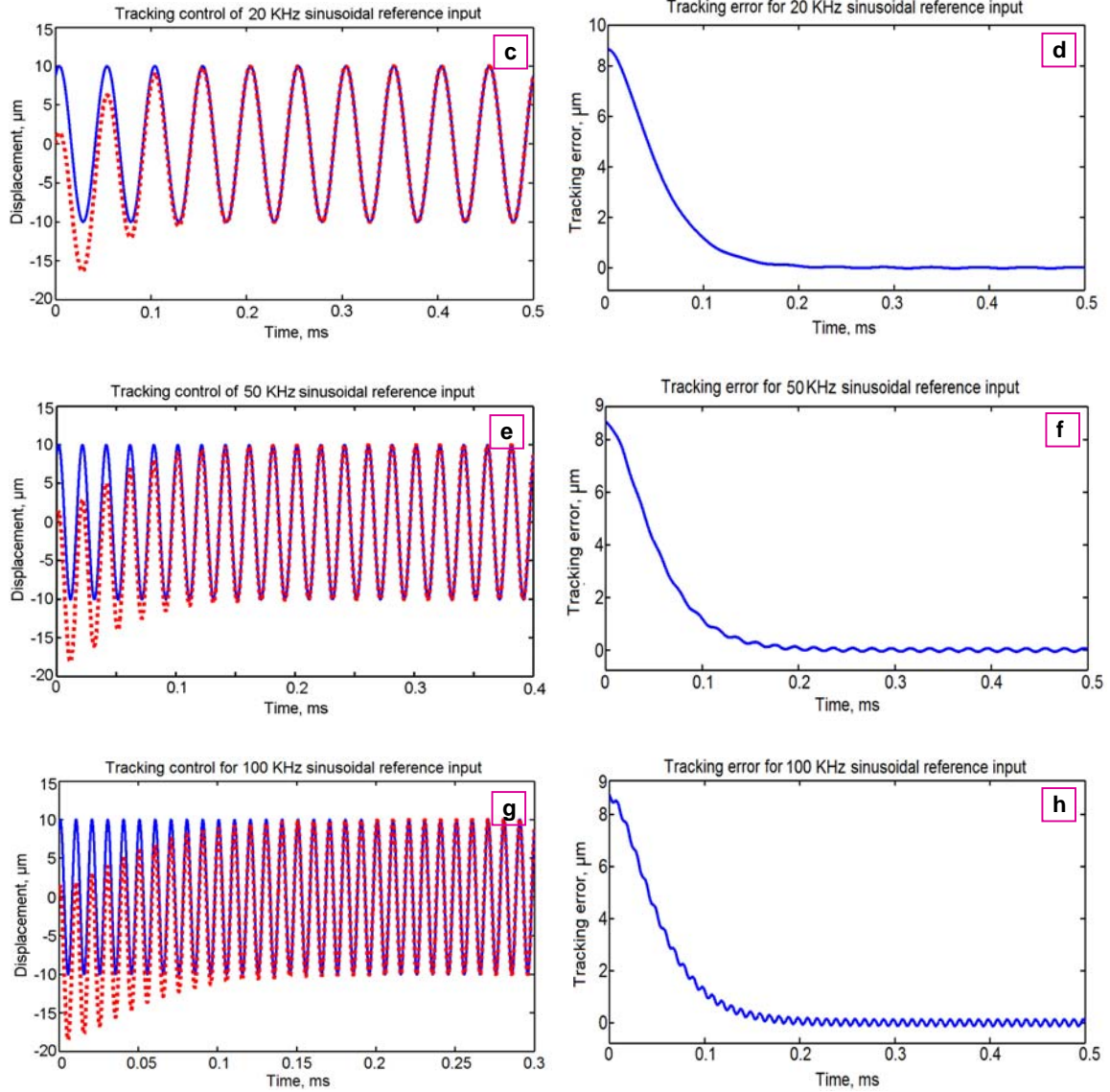


Figure 3.2 Tracking control results for 1, 20, 50 and 100 kHz sinusoidal desired trajectories using the proposed state-space controller.

3.1.2.1 Effects of tracking frequency on the controller performance

In practice, if there are no parametric uncertainties or unmodeled dynamics in the plant, the performance of the controller will be independent of the frequency of the desired trajectory; however, due to the ever-present numerical integration error in the simulations, the amplitude of tracking error increases with the frequency. Figure 3.3 depicts the steady state error trajectories

for 1, 20, 50 and 100 kHz desired trajectories. A linear increase with respect to frequency is observed for the tracking error as listed in Table 1.

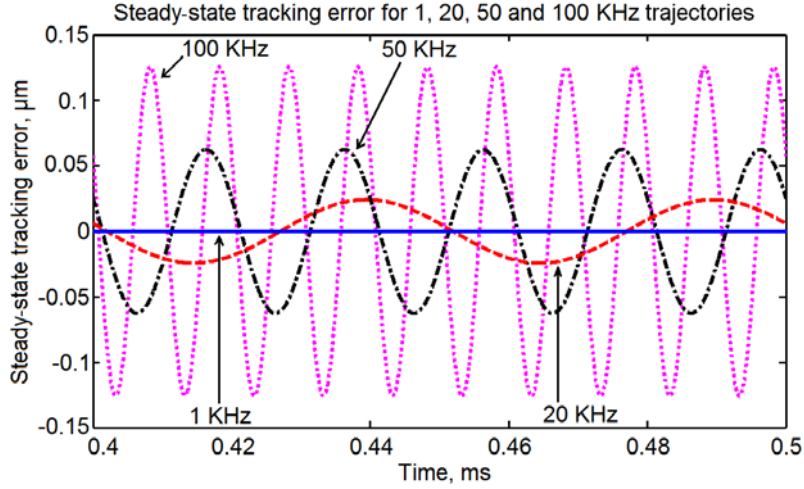


Figure 3.3 Steady state tracking error comparison, for 1, 20, 50 and 100 kHz sinusoidal trajectories.

Table 3.1 Steady state error at different tracking frequencies

Tracking frequency	1 kHz	20 kHz	50 kHz	100 kHz
Steady-state error	$1.46 \times 10^{-4} (\mu m)$ (0.0015%)	0.0247 (μm) (0.247%)	0.0625 (μm) (0.625%)	0.125 (μm) (1.250%)

3.1.2.2 Effect of control gains on the tracking performance

Controller gains have significant effect on the transient response as well as amplitude of the steady-state tracking error. As discussed in the previous subsections, the values of k_1 and k_2 are better to be selected in such a way that the error dynamics represent a critically damped behavior. Further increase in the values of k_1 and k_2 while keeping the error dynamics critically

damped shifts the poles further toward left on the s-plane. This suppresses the amplitude of steady-state error and decreases the settling time by making error dynamics stiffer. In practice, the gain values are limited by the actuator bandwidth and chattering; hence, poles cannot be shifted more toward left after a certain value.

Numerical simulations for the 100 kHz frequency tracking with three different pairs of control gains are carried out to demonstrate the effect of gains on the controller performance. It is clearly observed from Figure 3.4 that the steady-state amplitude as well as the settling time of tracking error decreases as the controller gains increases.

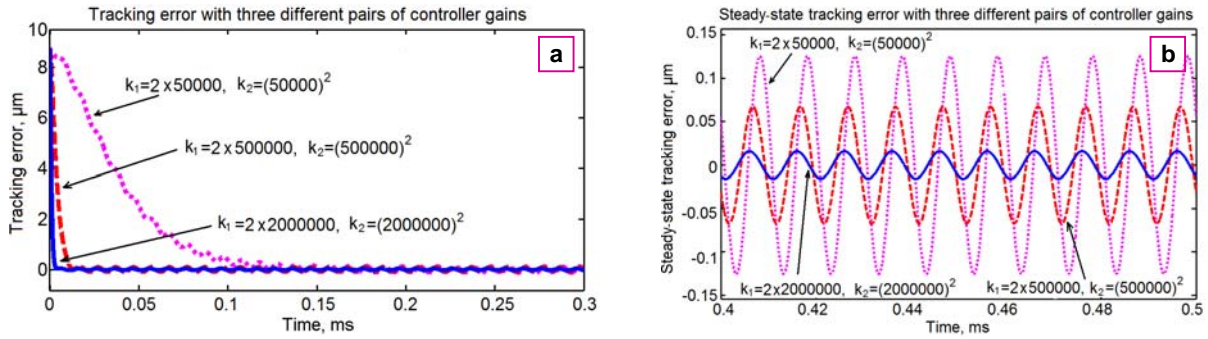


Figure 3.4 100 kHz frequency tracking errors using three different pairs of controller

3.2 Observer Development

For precise tracking control of the actuator displacement, the controller needs to have the accurate state feedback from the actuator. Since the states are the generalized coordinates of the rod and their time derivatives, it is impractical to directly measure them. However, state observers can be employed to estimate these unknown states. Since the system is stable, an open-loop observer can be the first attempt in the observer design. However, the presence of uncertainties and disturbances and large oscillations in the transient time necessitates the

implementation of feedback observers. This section discusses the development of optimal feedback observers for precise state estimation.

3.2.1 Observer design

For the stable state-space system given by Eq. (2.39), the following open-loop observer can be considered as an option for actuator states estimation:

$$\dot{\hat{x}}(t) = A\hat{x}(t) + Bu(t) \quad (3.13)$$

where \hat{x} represents the estimated actuator state vector. Due to the presence of parametric uncertainties in the plant, it is practically impossible to obtain accurate values of A and B matrices. This limitation of open loop observer eliminates its feasibility for accurate prediction of actuator states.

To minimize the state estimation error associated with inaccuracies in A and B matrices, the implementation of feedback observer is proposed as follows:

$$\dot{\hat{x}}(t) = \bar{A}\hat{x}(t) + \bar{B}u(t) + L(y(t) - C\hat{x}(t)) \quad (3.14)$$

where \bar{A} and \bar{B} are the nominal state and input matrices respectively and $y(t)$ is the axial tip displacement of the actuator, introduced as a feedback to the observer.

Appropriate selection of gain matrix L in Eq. (3.14) can leads to effective state estimation. To demonstrate the effects of matrix L on the closed-loop observer performance, the state estimation error is defined as:

$$\tilde{x}(t) = x(t) - \hat{x}(t) \quad (3.15)$$

By substituting the expression of real and estimated state derivatives from Eqs. (2.39) and (3.13) into equation (3.14), one can obtain:

$$\begin{aligned}
\dot{\tilde{x}}(t) &= Ax(t) - \bar{A}\hat{x}(t) + Bu(t) - \bar{B}u(t) - L(y(t) - C\hat{x}(t)) \\
&= Ax(t) - (A - \tilde{A})\hat{x}(t) + Bu(t) - (B - \tilde{B})u(t) - L(Cx(t) - C\hat{x}(t)) \\
&= (A - LC)(x(t) - \hat{x}(t)) + \tilde{A}\hat{x}(t) + \tilde{B}u(t) \\
&= (A - LC)\tilde{x}(t) + P(t)
\end{aligned} \tag{3.16}$$

where \tilde{A} and \tilde{B} represent the error between the actual and nominal state and input matrices respectively, and $P(t)$ represents the collective effect of system uncertainties which appears as a disturbance input to the closed-loop dynamics of observer error.

In order to minimize the amplitude and oscillations of the state observation error and to suppress the effect of the parametric uncertainties, the gain matrix L should be selected in such a way that all the eigenvalues of matrix $(A - LC)$ lie on the real axis, concentrated at one point and far from the imaginary axis in the left half-plane. Such an arrangement of eigenvalues represent a critically damped stiff error dynamics which suppresses the oscillations induced by uncertainties and decreases settling time of the estimation error. Appropriate selection of observer gain matrix is a critical step in achieving accurate estimation of the states.

3.2.2 Optimal selection of observer gain matrix

In practice, the rank of observability matrix $[C^T \mid A^T C^T \mid \dots \mid (A^T)^{2k-1} C^T]$ of the actuator is less than $2k$ (number of rows or columns of matrix A). Hence, the actuator is considered as unobservable system and there does not exist any observer gain matrix L which can force all poles of the system to be placed at any desirable location on the left half of s-plane. As a solution to this problem, a method for optimal placement of observer poles is proposed here. For this, an optimization algorithm is developed using Matlab to find a fairly good gain matrix L that forces all the eigenvalues of the observer to be as close as possible to desired location on the left half s-

plane. The cost function, on which the performance of the optimization algorithm depends, is a weighted function of real and imaginary distances of observer poles from the desired location.

Figure 3.5 depicts the results obtained from the optimal placement of observer poles at around -1000, -25000, and -50000 using the optimization algorithm. It is clear from Figure 3.5 that due to the unobservable plant, optimization algorithm is not able to concentrate all the eigenvalues, accurately at the desired locations.

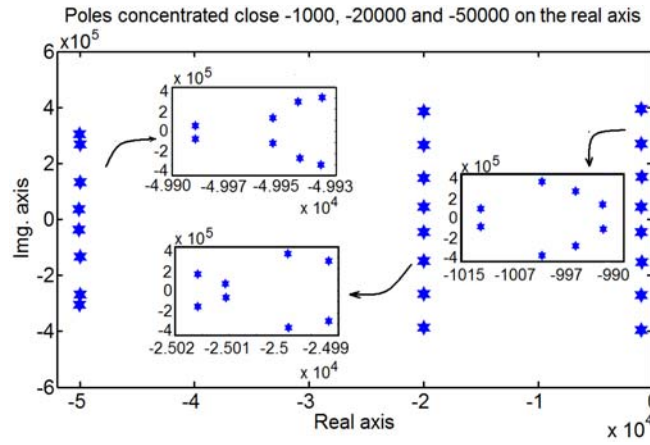


Figure 3.5 Results using optimization algorithm for concentrating the poles of the system at -1000, -20000 and -50000 on the real axis.

In order to reduce the settling time of the state estimation error, gain matrix (L) should be selected in such way that the poles of observer error dynamics are placed far from the imaginary axis in the left half s-plane, but in practice, the locations of these poles are restricted by the sampling time of the data acquisition system. As the poles move away from the imaginary axis in the left half s-plane, smaller sampling time is required to solve the observer differential equation. In the next section, numerical simulations are carried out for testing the credibility of the proposed observer design method.

3.2.3 Numerical validation of the observer

For the numerical validation of the observer, a combined four modes plant-observer Simulink model is developed as shown in Figure 3.6. The axial tip displacement ' $y(t)$ ' is given to the observer for accurate actuator state estimation. A numerical simulation has been carried out with the gain matrix L that concentrates the observer poles at -25000, and a 20 kHz sinusoidal input is applied to the plant. The results as shown in Figure 3.7 indicate the convergence of all observed states to those of the plant.

3.2.3.1 Effect of gain matrix on the observer performance

As discussed earlier, three different observer gain matrices L are determined using optimization algorithm, to place the eigenvalues of the observer at -10000, -25000 and -50000. Numerical simulations using these L matrices are performed to illustrate their effect on the observer performance. Figure 3.8 depicts the observation error for the 1st state of the system using three different observer gain matrices. The frequency of the applied plant input is set to 20 kHz.

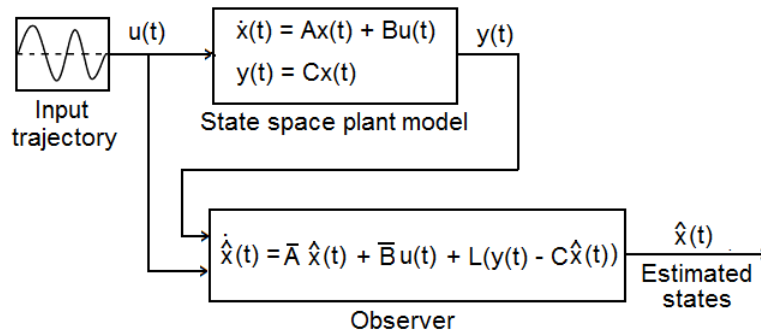


Figure 3.6 Observer/plant diagram for the accurate state estimation

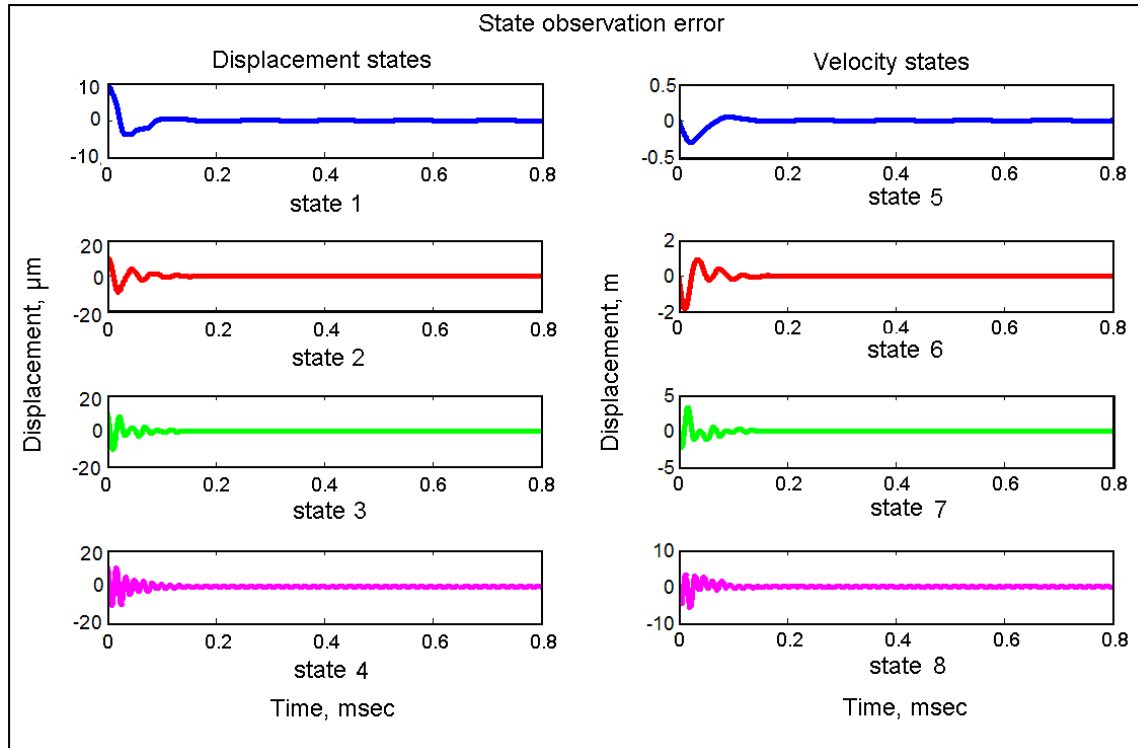


Figure 3.7 Convergence of the observer state estimation errors to zero.

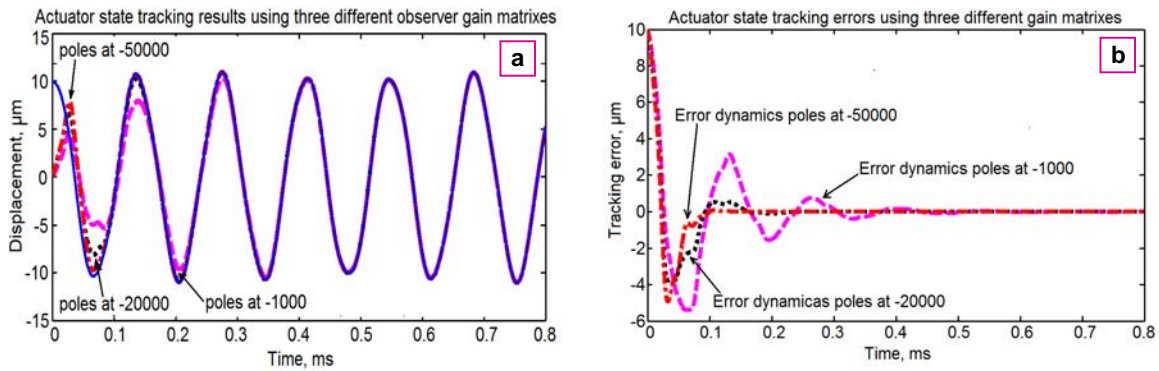


Figure 3.8 state estimation for three different observer gain matrices.

It is clear from Figure 3.8 that as the poles of the observer are moved toward left through the proper selection of observer gain matrix, the settling time of the observer error decreases, but as mentioned earlier, it will be limited by the sampling time of data acquisition system in practice.

3.3 State-Space Controller with Observer

In practice, both controller and observer need to be assembled together for real-time control of the plant. Figure 3.9 depicts the controller-observer diagram developed for the actuator control. In this strategy, the axial tip displacement of the actuator is input to the observer and the observer estimated states are fed back to the controller to generate the desired controlled input.

3.3.1 Numerical validation of the assembled controller and observer

For validation of combined controller-observer design, numerical simulations with four different tracking frequencies are carried out. In order to incorporate the parametric uncertainty in the simulations, the controller and the observer were built based on 5% perturbed plant parameters.

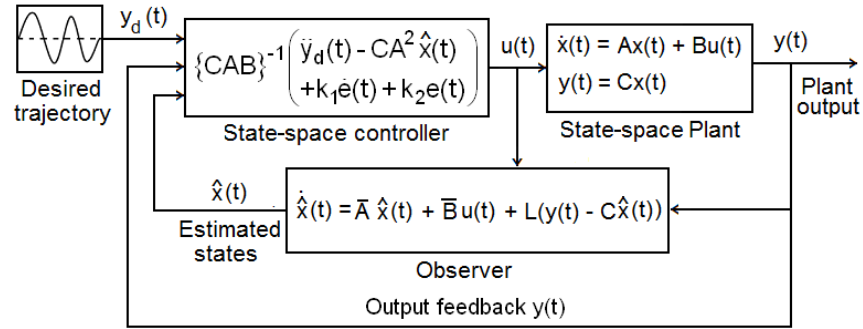
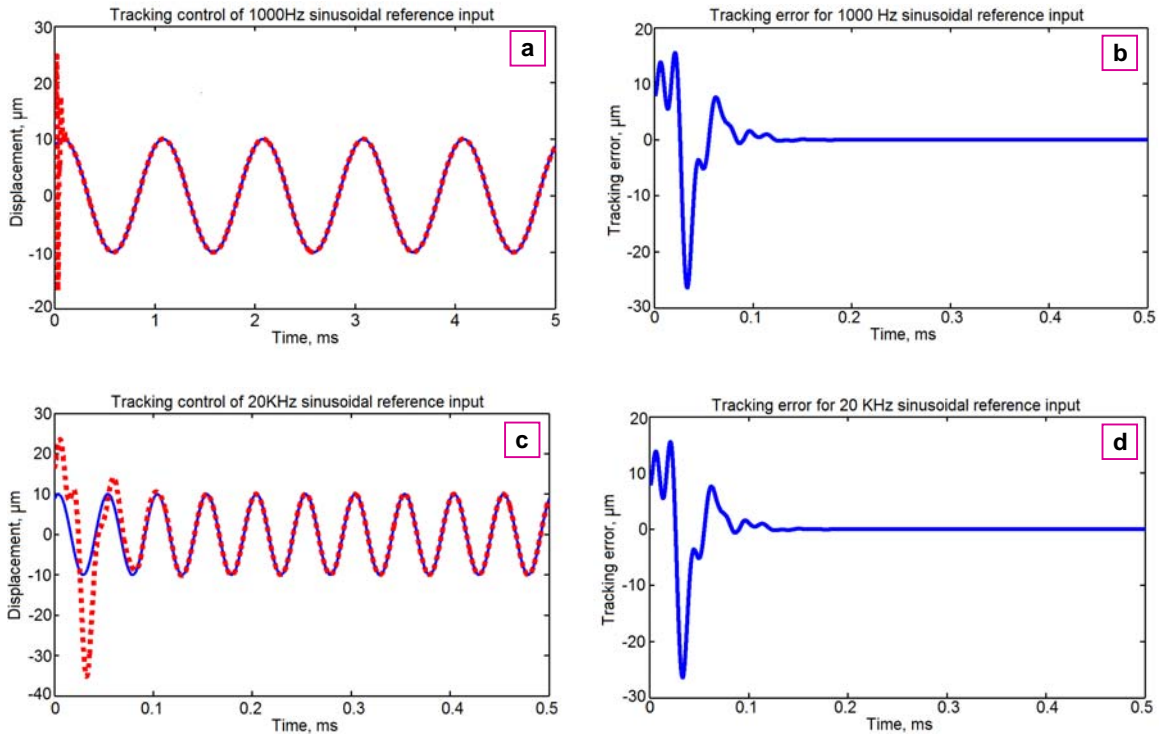


Figure 3.9 Integrated controller/observer diagram for precise plant control.

Figure 3.10 depicts the tracking results for 1, 20, 50 and 100 kHz sinusoidal desired trajectories. The controller gains (k_1 and k_2) and sampling time used for the simulations are set to 70000, 1.225×10^9 , and 10^{-8} sec, respectively. The observer gain matrix L is selected in such a way that

the poles of the observer placed close to -25000 on the real axis. As seen from Figure 3.10, all the trajectories converge to their desired reference.

The steady-state errors associated with 1, 20, 50 and 100 kHz sinusoidal reference inputs are enlarged and depicted in Figure 3.11. Because of the present 5% parametric uncertainties in the controller and observer design, the steady-state tracking error amplitude shown in Figure 3.11 increases with increase in frequency of the reference input. In order to decrease the steady-state error amplitude and to suppress the effect of parametric uncertainties on the tracking error, the values of controller gains should be increased, and consequently the observer gain matrix should be selected in such a way that the observer poles move more away from the imaginary axis in the left half s-plane.



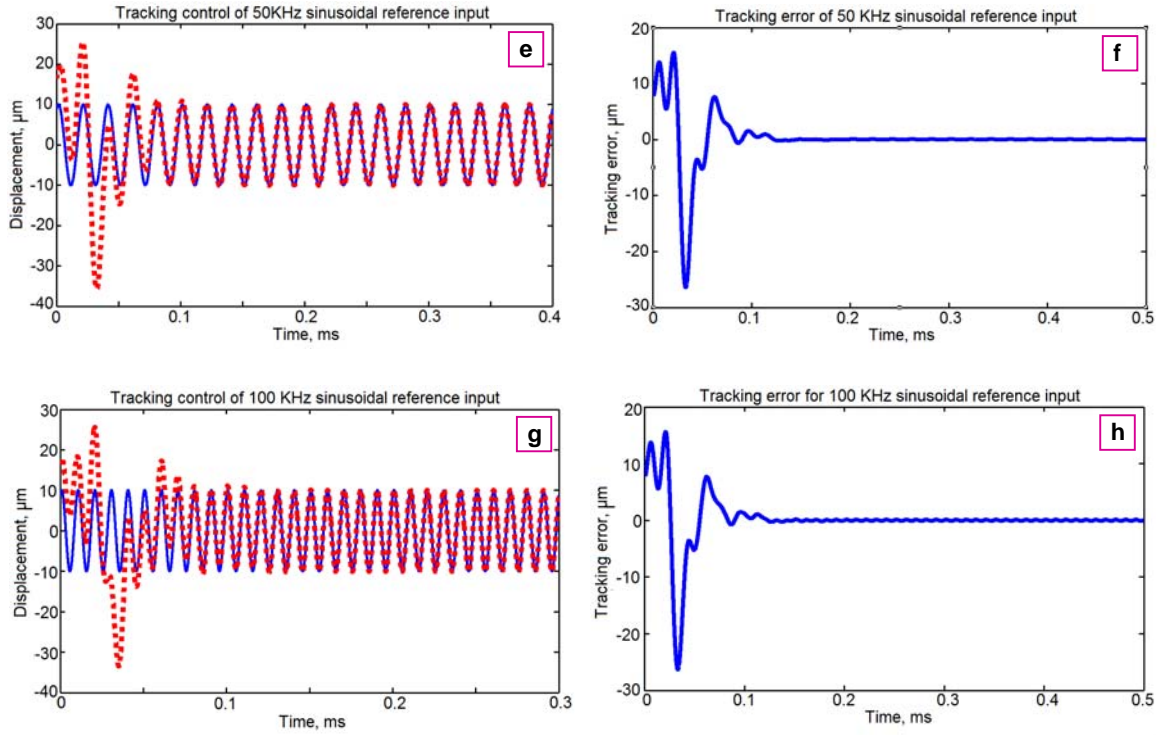


Figure 3.10 Tracking control results for 1, 20, 50 and 100 kHz sinusoidal reference inputs using combined controller/observer strategy.

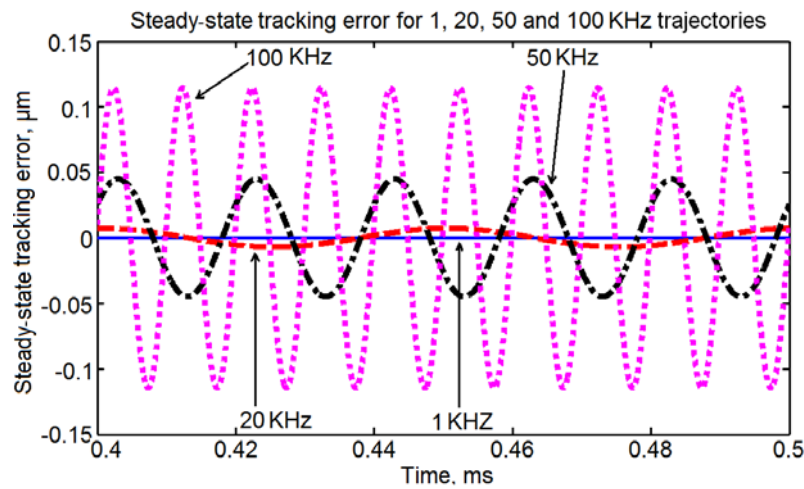


Figure 3.11 Steady state tracking error comparison for 1, 20, 50 and 100 kHz sinusoidal desired trajectories.

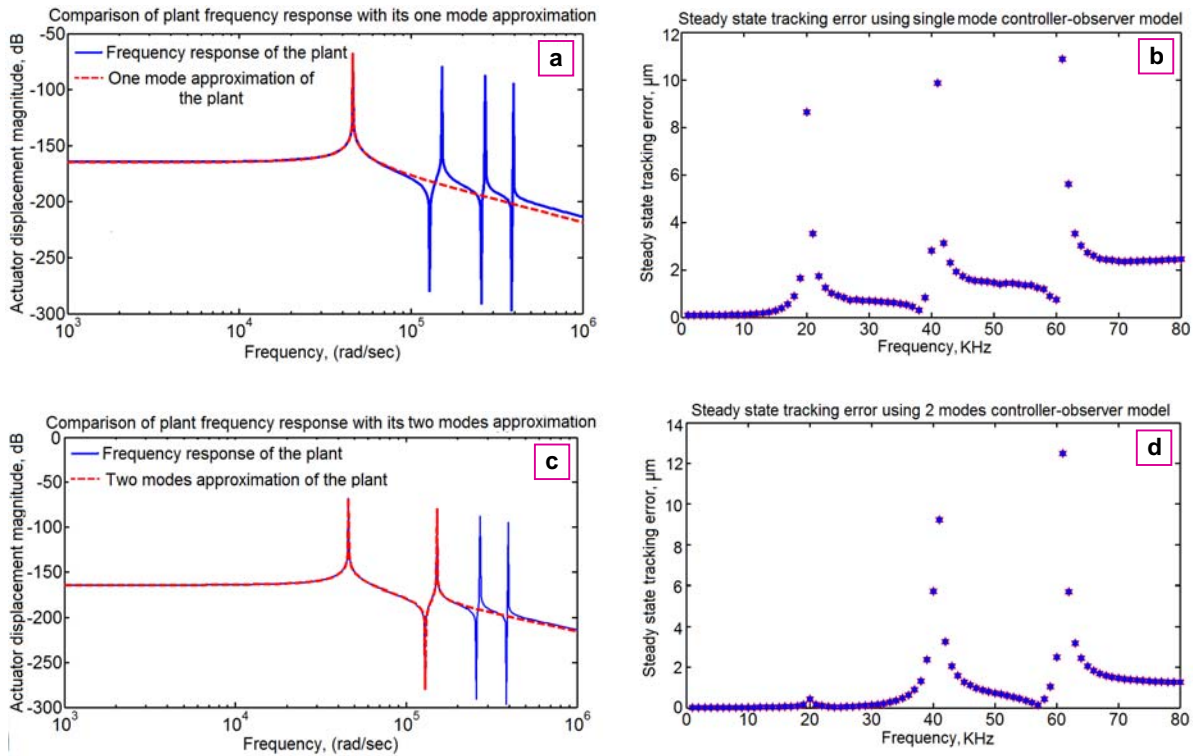
3.3.2 Effect of modes defeciancy on the tracking performance

In order to demonstrate the effect of the number of modes on the tracking performance over a frequency range, a set of numerical simulations have been carried out with modes defeciant controller/observers. The frequency response of the four-mode plant is compared with its one, two and three-mode approximations in Figure 3.12 (a), (c), (e), and (g), respectively. Sinusoidal desired trajectories having frequencies ranging from 1 to 80 kHz are applied to these four different controller/observer schemes that are developed based on 1, 2, 3 and 4 modes approximation of the plant. Results are depicted in Figure 3.12 (b), (d), (f), and (h), respectively. The frequency response of the single mode approximation of the plant matches the four-mode plant frequency response till 12 kHz as shown in Figure 3.12(a). It can be also observed from the error plot depicted in Figure 3.12(b) that the tracking bandwidth of controller/observer developed based on the single mode approximation is approximately 12 kHz which includes the first natural frequency of the actuator. The system is unable to precisely track the desired trajectory after 12 kHz.

The steady-state error peaks at second, third and fourth natural frequencies in Figure 3.12(b) depict the poor control performance of the single mode controller/observer for frequencies above the first resonance. Similarly, the tracking bandwidth of the two and three modes controller-observer model is approximately limited to 30 kHz and 50 kHz, respectively. It can, therefore, be concluded that precise tracking control of flexible rod-like actuators for any desired bandwidth is attained through the proposed control law, provided that all the resonant modes within that bandwidth are included in the state-space matrices used in the control structure.

3.3.3 Effect of controller gains on the steady state tracking error

To demonstrate the effect of controller gains on the amplitude of steady state tracking error, the controller/observer structure developed based on the first two modes of plant is simulated with two different sets of controller gain values for 1-80 kHz frequency range. As depicted in Figure 3.13, a considerable decrease in the steady-state tracking error is observed as the natural frequency of the error dynamics is increased from 500,000 rad/sec to 1,50,0000 rad/sec through the controller gains.



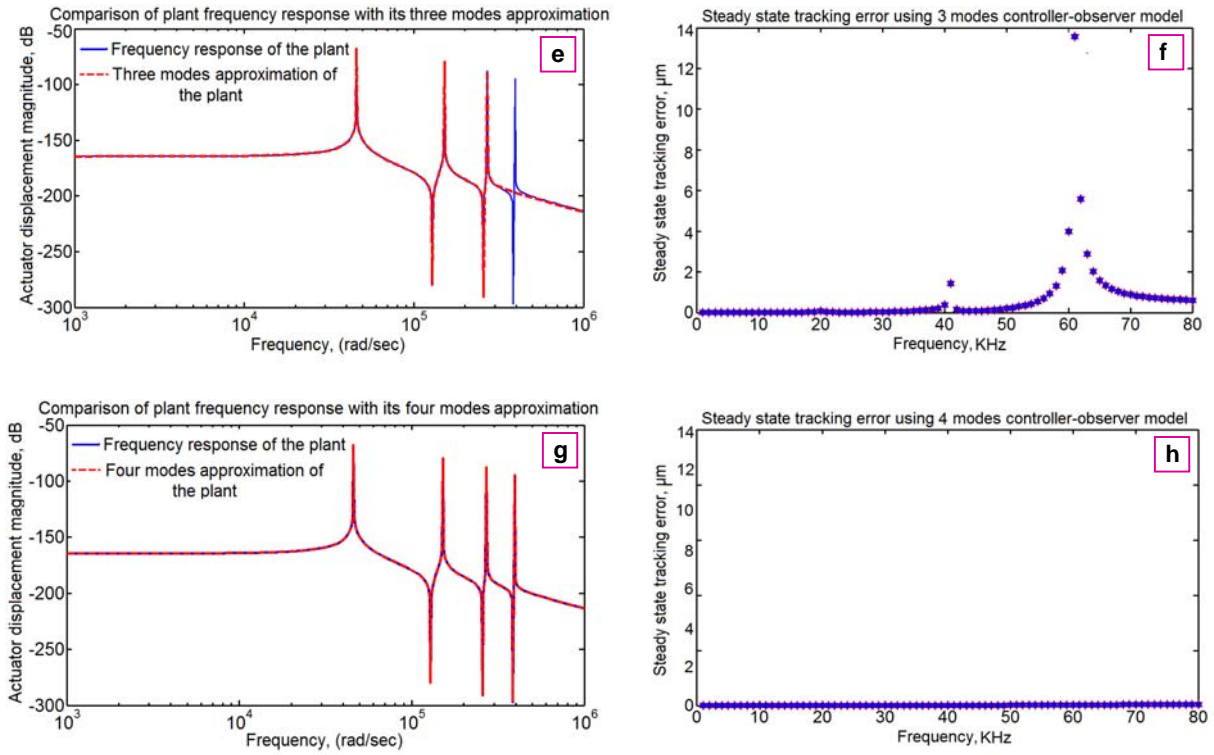


Figure 3.12 Different approximations and tracking control results for a (a, b) 1-mode; (c, d) 2-mode; (e, f) 3-mode; (g, h) 4-mode (full) representation of the system

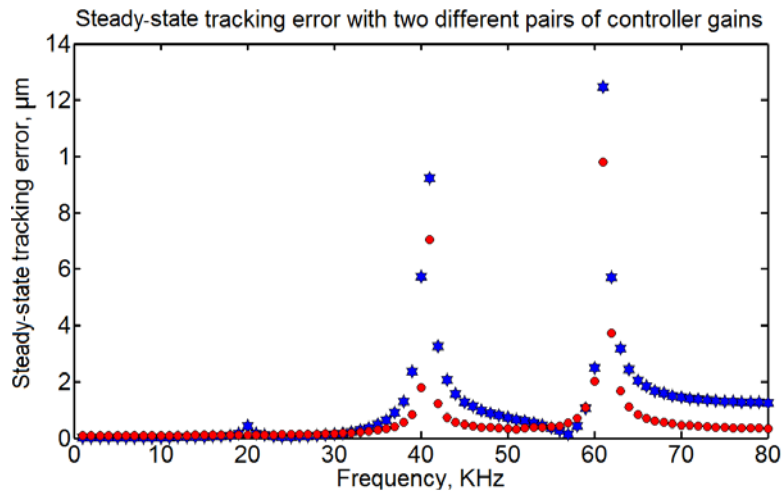


Figure 3.13 Steady-state tracking error comparisons for two different sets of controller gains for controller/observer based on two modes approximation.

3.4 Robust Control of the Galfenol Actuator

Due to the present inaccuracies in the plant parameters, the controller error dynamics given by Eq. (3.12) is modified as:

$$\ddot{e}(t) + k_1 \dot{e}(t) + k_2 e(t) = Gd \quad (3.17)$$

Because of the parametric uncertainty ' Gd ' in Eq. (3.17), the steady-state tracking error of the actuator cannot converge to zero with the use of the control law given in Eq. (3.11). In order to ensure zero convergence of steady-state error, a robustness feature needs to be incorporated into the controller design.

A hard switching sliding mode control that forces the steady-state error to be zero in the presence of parametric uncertainties is developed in this section. Due to the infeasibility of sliding mode control in practical implementation, it is replaced with a soft switching variable structure control. Robustness condition for the variable structure controller is defined in the form of controller gains and numerous simulations are carried out to tune these gains.

3.4.1 Sliding mode controller design

The state space representation of the plant with parametric uncertainty can be given as:

$$\begin{aligned} \dot{x}(t) &= Ax(t) + Bu(t) + Gd(t) \\ y(t) &= Cx(t) \end{aligned} \quad (3.18)$$

where $y(t)$ represents the axial tip displacement of the actuator, A and B are plant state space matrices, C is the output matrix and $Gd(t)$ represents the plant parametric uncertainty.

For actuator tip to follow the desired trajectory y_d , the tracking error of the closed loop system can be represented as:

$$e(t) = y_d(t) - y(t) \quad (3.19)$$

The first order time derivative of Eq. (3.12) yields:

$$\dot{e}(t) = \dot{y}_d(t) - \dot{y}(t) = \dot{y}_d(t) - C\dot{x}(t) = \dot{y}_d(t) - CAx(t) - CBu(t) - CGd(t) \quad (3.20)$$

As discussed in the previous section, for rod-like actuators, the coefficient of control input $u(t)$ (term CB in Eq. (3.9)) always remains zero. Therefore, the first order state-space controller cannot be used for the accurate tracking of actuator tip displacement.

The second order time derivative of the tracking error represented in Eq.(3.19) can be represented as:

$$\ddot{e}(t) = \ddot{y}_d(t) - CA^2x(t) - CABu(t) - CAGd(t) - CG\dot{d}(t) \quad (3.21)$$

Claim 3.2: For the plant given by Eq. (3.18), the control law $u(t)$ that ensures the asymptotic zero convergence of steady-state tracking error despite the plant parametric uncertainties is represented as:

$$u(t) = (CAB)^{-1}(\ddot{y}_d(t) - CA^2x(t) + \sigma\dot{e}(t) + \eta_1s(t) + \eta_2 \operatorname{sgn}(s)) \quad (3.22)$$

To achieve both robustness and tracking control of the actuator simultaneously, condition $\sigma, \eta_1, \eta_2 > 0$ and $\|CG\dot{d}(t) + CAGd(t)\| \leq \eta_2$ should be satisfied.

The sliding manifold $s(t)$, present in Eq. (3.22) is selected as:

$$s(t) = \dot{e}(t) + \sigma e(t) \quad (3.23)$$

where constant σ in the Eq. (3.23) represents the slope of the sliding manifold while η_1 and η_2 are the controller gains.

Proof: By substituting of the control law given by Eq. (3.22) into the second order error dynamics (3.21), it can be modified as:

$$\ddot{e}(t) + \sigma\dot{e}(t) + \eta_1s(t) + \eta_2 \operatorname{sgn}(s(t)) + CAGd(t) + CG\dot{d}(t) = 0 \quad (3.24)$$

To prove the asymptotic stability of the closed loop system, a positive definite Lyapunov function is defined as:

$$V = \frac{1}{2} s^2(t) \quad (3.25)$$

First order time derivative of the Lyapunov function represented in Eq. (3.25) is given as:

$$\dot{V}(t) = s(t)\dot{s}(t) = s(t)(\ddot{e}(t) + \sigma\dot{e}(t)) \quad (3.26)$$

Substituting second order time derivative of error from Eq. (3.24), into Eq. (3.26) yields:

$$\dot{V}(t) = -\eta_1 s^2(t) - \eta_2 s(t) \operatorname{sgn}(s(t)) - (CAGd(t) + CG\dot{d}(t))s(t) \quad (3.27)$$

$$\dot{V}(t) = -\eta_1 s^2(t) - \eta_2 |s(t)| - (CAGd(t) + CG\dot{d}(t))s(t) \quad (3.28)$$

If the controller gains are chosen in such a manner that $\|CG\dot{d}(t) + CAGd(t)\| \leq \eta_2$ and $\eta_1, \eta_2 > 0$ remains true in the first order time derivative of positive definite Lyapunov function given by Eq. (3.28), conditions $\eta_2 |s(t)| \geq (CAGd(t) + CG\dot{d}(t))s(t)$ and $\eta_1 s^2(t) \geq 0$ are satisfied and $\dot{V}(t)$ remains negative semi definite ($\dot{V}(t) \leq 0$) for all $t > 0$. This ensures the asymptotic zero convergence of $e(t)$ and $\dot{e}(t)$ using invariant set theorem.

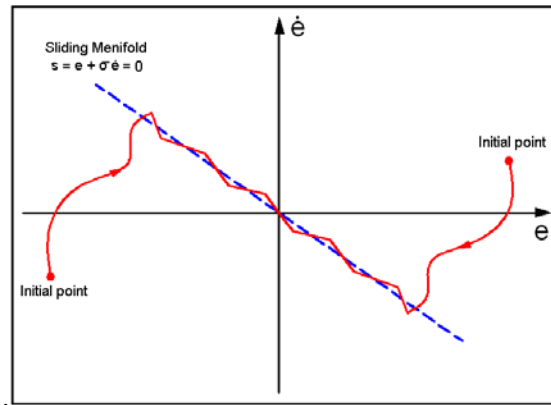


Figure 3.14 Graphical representation of sliding mode control

Graphical representation of the sliding mode control depicted in Figure 3.14 represents the zero convergence of $e(t)$ and $\dot{e}(t)$ starting from an initial location along the sliding manifold $s(t) = \dot{e}(t) + \sigma e(t) = 0$ with the decreasing rate of σ .

3.4.2 Replacement of sliding mode control by soft switching variable structure control

The hard switching signum function used in the sliding mode control law given by Eq. (3.22) causes chattering of the error along the sliding manifold as depicted in Figure 3.14. In order to remove this chattering phenomenon, the signum function is replaced with the soft switching saturation function, equipped with the small positive coefficient ε that controls the chattering rate.

Claim 3.3: For the plant represented in Eq. (3.18), the variable structure control law that ensures the asymptotic stability of the closed loop system in the presence of parametric uncertainty is defined as:

$$u(t) = (CAB)^{-1} \left(\ddot{y}_d(t) - CA^2x(t) + \sigma \dot{e}(t) + \eta_1 s(t) + \eta_2 \text{sat}(s(t)/\varepsilon) \right) \quad (3.29)$$

The saturation function used in above control law is given as:

$$\text{sat}(s/\varepsilon) = \begin{cases} s/\varepsilon & \text{for } |s| < \varepsilon \\ \text{sgn}(s) & \text{for } |s| \geq \varepsilon \end{cases} \quad (3.30)$$

If the robustness conditions $\sigma, \eta_1, \eta_2 > 0$ and $\|CG\dot{d}(t) + CAGd(t)\| \leq \eta_2$ are satisfied, then the steady-state tracking error must be bounded in the region, defined as $|s(t)| < \frac{\eta_2 \varepsilon}{\eta_1 \varepsilon + \eta_2} < \varepsilon$ at

$t \rightarrow \infty$.

Proof: Assuming that the sliding variable $s(t)$ starts from an initial location depicted in Figure 3.15.

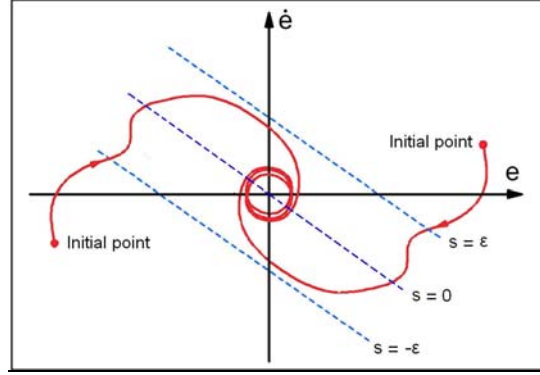


Figure 3.15 Graphical representation of variable structure control

As $s(t)$ starts from a point outside the boundary of ε , condition $|s| \geq \varepsilon$ in Eq. (3.30) is satisfied.

In this situation the variable structure control law given by Eq. (3.29) behaves the same as the sliding mode control presented in Eq. (3.22), that forces the sliding function towards the origin into the region defined by $s(t) = \pm \varepsilon$, as depicted in Figure 3.15. As the sliding function reaches inside the boundary ε , the structure of the control law given by Eq. (3.29) modified to:

$$u(t) = (CAB)^{-1} \left(\ddot{y}_d(t) - CA^2x(t) + \sigma \dot{e}(t) + \eta_1 s(t) + \eta_2 s(t)/\varepsilon \right) \quad (3.31)$$

The first order time derivative of the positive definite Lyapunov function for the control law given by Eq. (3.31) is defined as:

$$\dot{V}(t) = -\eta_1 s^2(t) - \eta_2 s^2(t)/\varepsilon - (CAGd(t) + CG\dot{d}(t))s(t) \quad (3.32)$$

$$\dot{V}(t) = - \left[\left(\eta_1 + \eta_2/\varepsilon \right) s(t) + (CAGd(t) + CG\dot{d}(t)) \right] s(t) \quad (3.33)$$

If sliding function stays inside the boundary of ε such that condition

$$\frac{|CAGd(t) + CG\dot{d}(t)|\varepsilon}{\eta_1\varepsilon + \eta_2} \leq |s(t)| \leq \varepsilon \text{ is satisfied, then the first order time derivative of Lyapunov}$$

function given by Eq. (3.33) will remain negative semi definite ($\dot{V}(t) \leq 0$) and will force $s(t)$ to move further toward origin. As $s(t)$ enters inside the region

$$|s(t)| < \frac{|CAGd(t) + CG\dot{d}(t)|\varepsilon}{\eta_1\varepsilon + \eta_2} \leq \frac{\eta_2\varepsilon}{\eta_1\varepsilon + \eta_2} < \varepsilon, \text{ the first order time derivative of Lyapunov function}$$

can become positive and will try to throw the sliding function out of this region. Outside this region, again the condition $\dot{V}(t) \leq 0$ will be satisfied and $s(t)$ will be again forced towards the origin. Sliding function $s(t)$ will finally settle down in to the region of convergence defined by

$$|s(t)| < \frac{\eta_2\varepsilon}{\eta_1\varepsilon + \eta_2} < \varepsilon.$$

3.4.3 Numerical validation of the variable structure control

To experimentally validate the variable structure control, a 50 kHz sinusoidal input tracking is carried out using Matlab/Simulink. The simulation results are depicted in Figure 3.16. In order to satisfy the robustness condition as well as to achieve the rapid error reduction rate, controller gain η_2 and slope σ of the sliding plane are chosen to be 55000 and 200000, respectively. To entrap the steady state error within a small range, the value of ε is selected as 0.01.

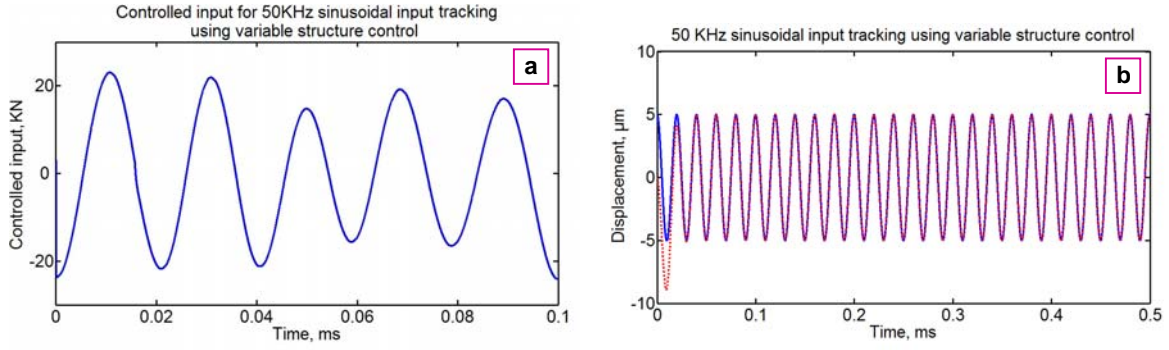
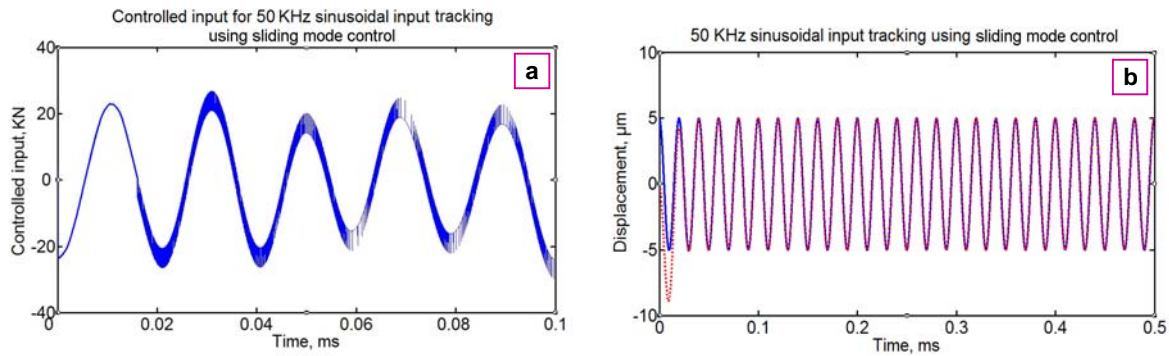


Figure 3.16 50 kHz sinusoidal desired input tracking using variable structure control, (a) controll input applied to the plant, and (b) tracking result

It is clear from Figure 3.16 that the variable structure control gives accurate tracking results for high frequency desired input in the presence of parametric uncertainties.

3.4.4 Comparison of variable structure control with the sliding mode control

To compare the performance of variable structure controller with the sliding mode control, numerical simulations with 50 kHz sinusoidal input tracking are performed. Figure 3.17 (a, b) depicts the tracking result using sliding mode control. Phase portrait results using both the controllers are depicted in Figure 3.17(c).



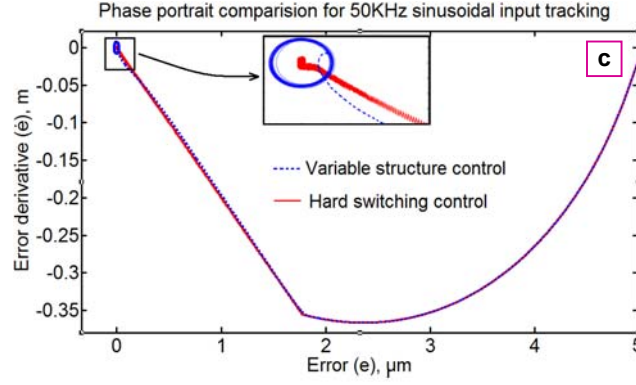


Figure 3.17 50 kHz sinusoidal reference input tracking using sliding mode control; (a) control input applied to the plant, (b) tracking result, and (c) phase portrait comparison of variable structure control with hard switching sliding mode control

It is clear from the limit cycle in case of variable structure control depicted in Figure 3.17 (c), that the hard switching sliding mode control has the definite advantage over variable structure control with soft switching because of the zero convergence of the steady-state error, but the chattering of the error due to the abrupt switching of control input depicted in Figure 3.17 (a) limits its practical implementation.

3.4.5 Gain tuning of variable structure controller

For the high frequency desired input tracking, appropriate gain tuning of the variable structure controller is very essential. In order to obtain the accurate tracking results, controller gain η_2 should be chosen large enough in order to satisfy the robustness condition given by $\eta_2 > 0$ and $\|CG\dot{d}(t) + CAGd(t)\| \leq \eta_2$. Numerical simulations with two different η_2 values are carried out using Simulink. The value of η_1 for the simulations is chosen to be zero.

Figure 3.18 depicts the phase portrait results for $\eta_2 = 35000$ and 55000 respectively. It is clear from Figure 3.18(a) that because of not satisfying the robustness condition, the sliding

plane $s(t)$ goes out of the bounds of $s(t) = \pm \varepsilon$. By increasing the magnitude of η_2 from 35000 to 55000 in Figure 3.18(b), the robustness condition of the controller is satisfied and sliding plane converges to limit cycle that is in to the zone of $s(t) = \pm \varepsilon$. The other controller parameters ε, σ used in the simulation are chosen as 0.01 and 200000, respectively.

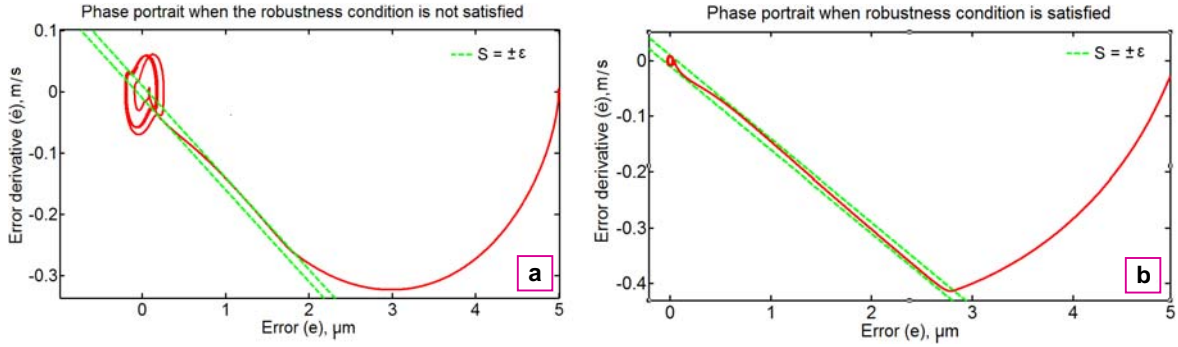


Figure 3.18 Effect of robustness condition on the variable structure control; (a) phase portrait when robustness condition is satisfied, and (b) phase portrait when robustness condition is not satisfied

Apart from satisfying the robustness condition, performance of variable structure control with soft switching depends on the value of ε . As proved in Claim 3.2 if the robustness condition of the controller is satisfied, the steady-state tracking error of the closed loop system always converges to the limit cycle bounded in the region of convergence given as

$$|s(t)| < \frac{\eta_2 \varepsilon}{\eta_1 \varepsilon + \eta_2} < \varepsilon. \text{ To observe the effect of } \varepsilon, \text{ a set of simulations for 50 kHz sinusoidal}$$

frequency tracking are carried out with two different values of ε as 0.05 and 0.1, respectively.

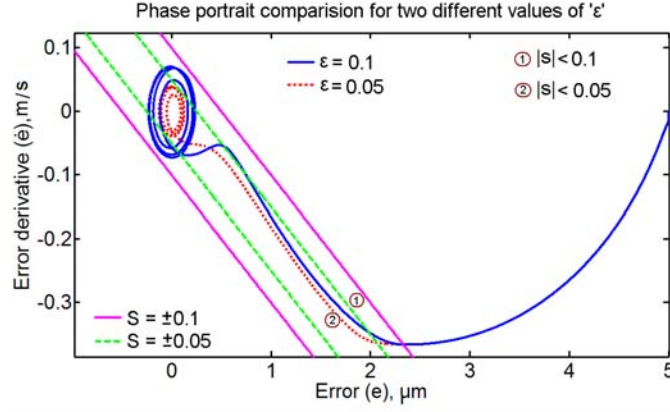


Figure 3.19 Effect of ε on the soft switching variable structure control

The decreasing radius of the limit cycle for lesser value of ε depicted in Figure 3.6 implies the improvement in the steady-state error. The values of η_1, η_2 and σ for the simulations are kept constant as 0, 55000 and 200000, respectively.

In order to observe the effect of σ on the performance of variable structure controller, 50 kHz sinusoidal input tracking is carried out with two different values of σ . Figure 3.20 depicts the phase portrait with values of σ as 15000 and 25000, respectively.

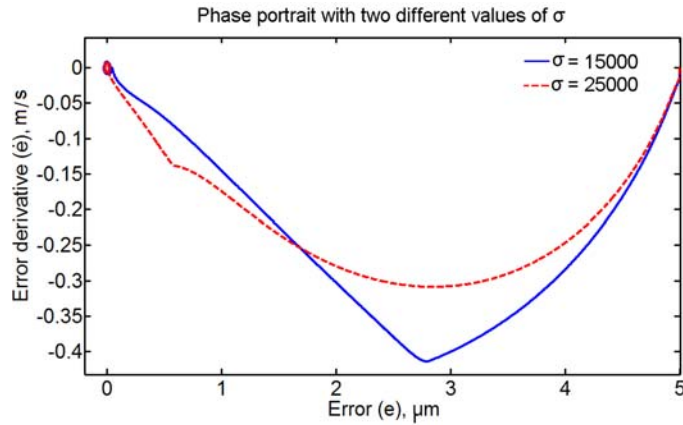


Figure 3.20 Effect of σ on the soft switching variable structure control

Due to the fact of heaving sliding manifold as $s(t) = \dot{e}(t) + \sigma e(t) = 0$, the zero convergence rate of the error in Figure 3.20 increases with increase in σ . The controller gains η_1, η_2 and ε for the simulations are chosen to be 0, 55000 and 0.01, respectively.

In order to achieve precise motion-control of the rod-like solid state Galfenol actuator, the multi-loop hysteresis nonlinearity is controlled along with actuator dynamic behavior control. Hysteresis predictive modeling framework utilizing memory based nonlinear mapping technique is developed in Chapter 4. Also, the hysteresis compensation technique utilizing Proportional-Integral (PI) control is used in order to achieve accurate hysteresis control.

CHAPTER 4

HYSTERESIS MODELING AND COMPANSATION[§]

4.1 Introduction

Despite of all the advantages, Galfenol does exhibit magnetic saturation, magnetic hysteresis and magnetomechanical nonlinearities, and hence accurate models describing the effect of magnetic field on strain are necessary for device design and control. To that end, a set of descriptive memory-based properties has been recently proposed providing sufficient knowledge for precise prediction of major and minor hysteresis loops. This approach has been validated for hysteresis nonlinearity in piezoelectric actuators. It has been shown that for precise prediction of hysteresis, a number of memory units must be included in the model to record key points of past hysteresis trajectories and use them for prediction of future paths. The proposed model has shown to offer better accuracy and improved computational efficiency compared to other existing methods.

Building on the memory-based approach, a generalized framework is proposed in this chapter for modelling the highly nonlinear multiple-loop hysteresis behaviour of Galfenol micro-positioning actuators. The model separates the nonlinearity from the hysteresis looping effect, and approximates it with an exponential average function. Using the memory-based properties of hysteresis, a formulation is then derived in which the average function is incorporated in

[§]The content of this chapter may have come directly or indirectly from our joint publication: [Bashash S., Vora K., Jalili N., Evans P. G., and Dapino M., "Memory-based hysteresis compensation and nonlinear modeling of Galfenol-driven micro-positioning actuators," in *Proceedings of 1st ASME Dynamic Systems and Control Conference, October 2008, Ann Arbor, MI.*]

development of hysteresis loops. The proposed model is experimentally identified and validated for a Galfenol actuator. Results indicate good agreement of the model response with the experimental data in predicting both major and minor loops. The advantages of the model over the existing methods include computational and parametric efficiency, simplicity of identification, and accuracy of response.

4.2 Experimental Setup and Results

To investigate the memory-based behavior of Galfenol actuators, a set of experiments has been carried out. An experimental setup comprising a Galfenol-driven actuator is used as shown in Figure 4.1.

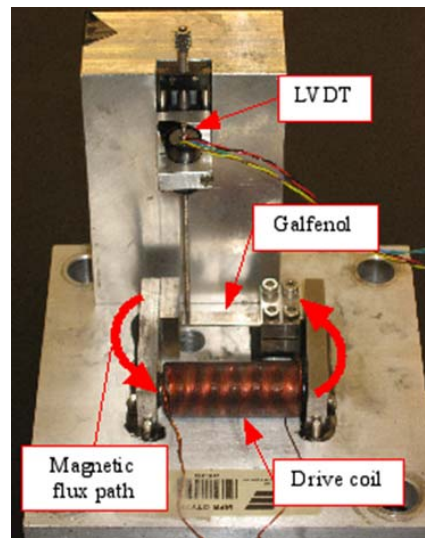
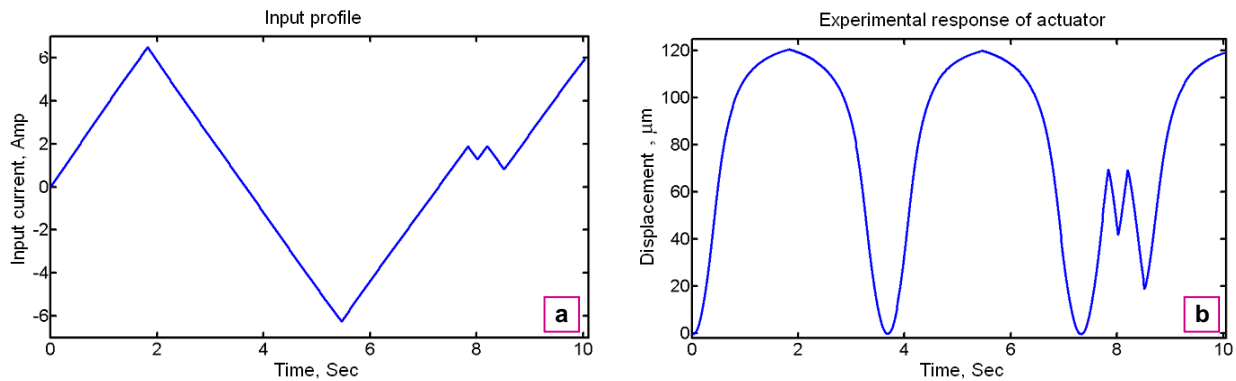


Figure 4.1 Experimental setup for a Galfenol-driven micro-positioning actuator.

This setup was prepared and developed at Ohio state university as a part of ongoing collaboration. A unimorph beam consisting of a Galfenol laminate bonded to a brass laminate is placed in a magnetic circuit composed of steel flux paths driven by a copper coil. Both laminates have dimensions $1'' \times 0.25'' \times 0.015''$ and were bonded with Armstrong A12 adhesive. The

Galfenol is research grade $\text{Fe}_{81.6}\text{Ga}_{18.4}$ which has been stress-annealed in order to pre-align magnetic domains perpendicular to the length of the beam thereby providing optimal magnetostriction (~ 200 ppm) along the beam length. When the coil is energized, a magnetic field causes the Galfenol to elongate while the brass laminate causes it to bend by restricting its elongation along the contact face. The coil is driven by an AE Techron LVC 5050 Linear Amplifier operated in voltage control mode. Current measurements are provided by the amplifier at a gain of 20 A/V and displacements are measured by a linear variable differential transformer (LVDT) instrument having a gain of 0.0124742 in/V. The LVDT instrument comprises a Lucas Schaevitz MHR025 sensor and ATA-101 amplifier. A SignalCalc ACE dynamic signal analyzer from Data Physics Corporation simultaneously controls the drive coil amplifier and acquires the displacement and current measurements. Major and nested minor loop tests were conducted using ramp inputs with a rate of 6 V/sec and sampling frequency of 40 Hz. Closure of the minor loops suggests that dynamic effects are negligible at the frequency tested. Figure 4.2 depicts the response of the actuator to an input current signal with a triangular profile.



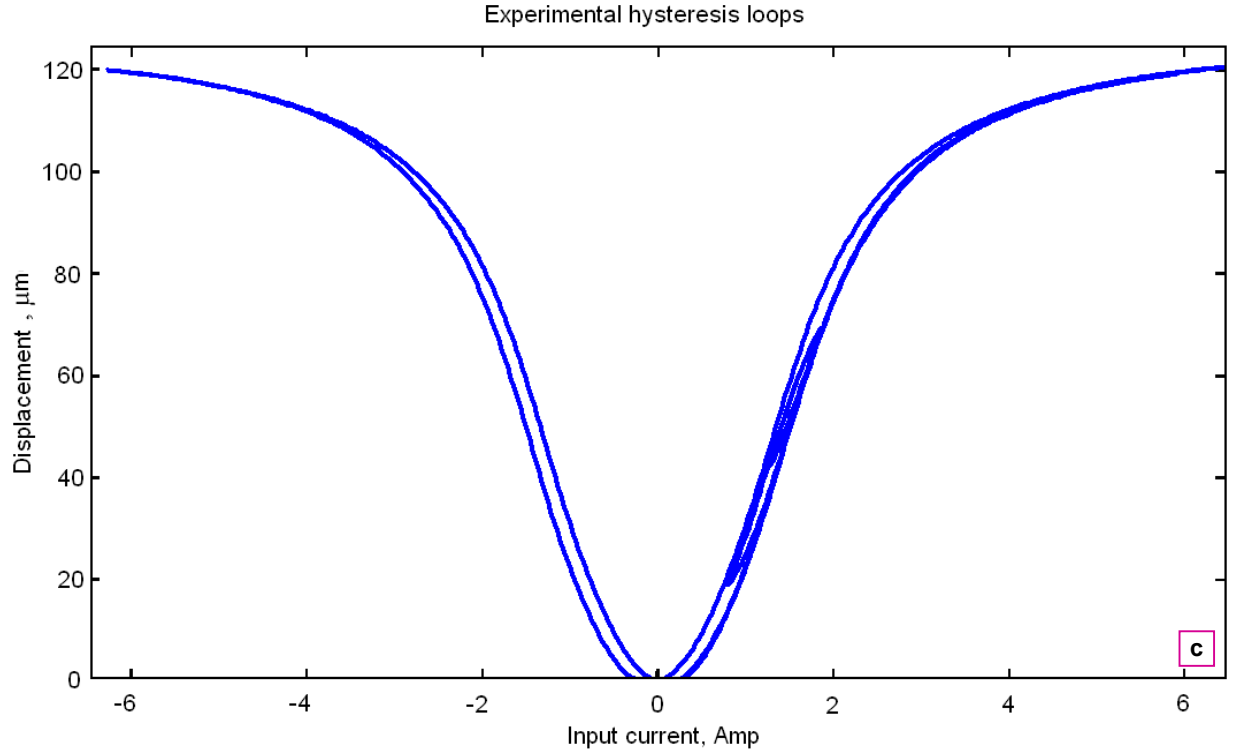


Figure 4.2 Nonlinear hysteretic response of Galfenol actuator: (a) Input current profile, (b) actuator displacement, and (c) butterfly-like hysteresis loops.

As seen in Figure 4.2(b)-(c), the response is nonlinear with a butterfly-shaped configuration and the looping effect due to magnetic hysteresis. While the saturation nonlinearity dominates over the hysteresis, precision control requirement requires that both be taken into account. From Figure 4.2(c), which shows the hysteresis loops between the applied current and the resulting displacement, two important characteristics are observed which will be applied to the modeling framework: (i) the hysteresis loops are symmetric with respect to the vertical axis, and (ii) the centre of the loops, where the ascending and descending curves cross each other, is located at the origin. Therefore, the butterfly configuration can be reduced to a single-sided hysteresis configuration without the loss of generality and for the sake of simplicity.

4.3 Modeling Nonlinearities using Average Curve Model

In this section, an exponential average curve fitting procedure is used to identify the best fit for the combined ascending and descending hysteresis curves. This method only predicts the nonlinearity of the response without considering its hysteresis looping effect. However, the obtained average function can be directly utilized in a generalized memory-based hysteresis modeling framework, as discussed in section 4.4.

4.3.1 Average Curve Model

A straightforward approach for eliminating the main source of inaccuracies due to the nonlinearities is to find an average curve between the ascending and descending reference curves as shown in Figure 4.3(a). Therefore, the model simply reduces to a single function between the applied current and the resulting displacement. The following exponential formulation precisely approximates the hysteresis average curve:

$$x = \bar{f}(v) = \sum_{i=1}^n (a_i v^{i-1}) \left[1 - \exp \left(- \sum_{j=1}^m b_j v^j \right) \right] \quad (4.1)$$

where v and x respectively represent the input current and output displacement, and a_i and b_j are constant shaping coefficients. Choosing appropriate polynomial orders m and n , a least square optimization can be used to identify the unknown shaping parameters based on a set of given experimental data.

4.3.2 Experimental Results and Numerical Simulations

Letting $n = m = 5$ in Eq. (4.1) to precisely approximate the experimental data, the following expression is obtained for the average function:

$$x = \bar{f}(v) = (a_1 + a_2v + a_3v^2 + a_4v^3 + a_5v^4) \left(1 - e^{(b_1v + b_2v^2 + b_3v^3 + b_4v^4 + b_5v^5)} \right) \quad (4.2)$$

The response of the average model with the input shown in Figure 4.2(a) is compared to the experimental response in Figure 4.3. The maximum error percentage and the average error are 5.0232% and 1.7602 μm , respectively. The induced error is due to the multi-path hysteretic response of the actuator; hence, a precise hysteresis model must be incorporated for acquiring higher precision, as will be discussed next.

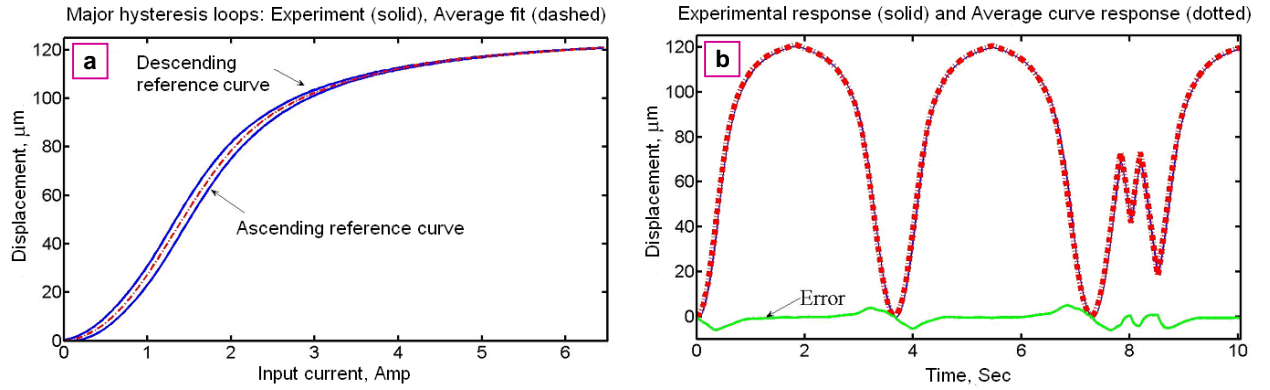


Figure 4.3 Response of average curve model: (a) the average curve between the ascending and descending hysteresis curves, and (b) comparison with the actuator response.

4.4 Memory-based Hysteresis Modeling

The memory-based hysteresis modeling framework, developed for piezoelectric actuators⁵⁻⁷, is proposed here to investigate the modeling feasibility of the Galfenol hysteretic behavior. This framework is based on three important properties: targeting of turning points, curve alignment and the wiping out effect, which enable precise prediction of the multiple-loop hysteresis response of active materials. To develop the memory-based hysteresis model for a Galfenol actuator, the nonlinearity of the response is separated from its looping behavior. Figure 4.4(a) demonstrates that ascending and descending hysteresis trajectories can share the nonlinearity from a single average curve that passes through them. However, to include the hysteresis effect, a mathematical mapping is utilized to split the average curve into appropriate ascending and descending trajectories. Before representing a mathematical formulation, a summary of hysteresis properties is reviewed in the following paragraph.

Starting from the origin, the *initial* hysteresis trajectory, when moving upward, targets the upper threshold point corresponding to the maximum possible input. Likewise, the first descending trajectory targets the lower threshold point corresponding to the minimum allowed input. When the direction of the input changes, the information of that turning point is recorded to be utilized for the prediction of future hysteresis paths. A hysteresis trajectory starting from a turning point approaches the closest recorded turning point on the opposite side. This property, termed targeting of turning points, enables the prediction of the hysteresis path between two subsequent turning points. When the trajectory hits a target point, the minor hysteresis loop associated with that point is closed and the properties of wiping-out and curve alignment occur simultaneously. The wiping-out effect implies that when a minor loop is closed, it is no longer useful for the prediction of future hysteresis paths. Therefore, the information of that loop and its

associated turning points can be eliminated from the memory unit. This property is advantageous as it helps to vacate the memory units from unnecessary information and keep them for recording the forthcoming turning points. Another advantage of the proposed framework is the curve alignment property observed at the turning points; that is the hysteresis trajectory changes path slightly and aligns to the previously broken curve associated with that turning point, and continues its path towards the next target point.

4.4.1 Mathematical formulation

To mathematically model a nonlinear and hysteretic response, we first focus on predicting a hysteresis track between a starting turning point (v_1, x_1) and its target point (v_2, x_2) . The following nonlinear mapping is proposed for this hysteresis track:

$$x_{12}(v) = x(v, v_1, x_1, v_2, x_2) = x_1 + k \left(1 + a e^{\tau(\bar{f}(v) - \bar{f}(v_1))} \right) (\bar{f}(v) - \bar{f}(v_1)) \quad (4.3)$$

where v represents the operator input (applied current in the case of a Galfenol actuator), a and τ are the mapping coefficients being separately identified for the ascending and descending curves, and \bar{f} stands for the average function given by Eq. (4.1). Coefficient k represents the relative slope of mapping and is expressed as:

$$k = \frac{x_2 - x_1}{(\bar{f}(v_2) - \bar{f}(v_1)) \left(1 + a e^{-\tau(\bar{f}(v_2) - \bar{f}(v_1))} \right)} \quad (4.4)$$

Substitution of Eq.(4.4) into Eq.(4.3) for the hysteresis track between point (v_l, x_l) and (v_2, x_2) yields:

$$x_{l2}(v) = x_1 + \frac{\left(1 + ae^{-\tau(\bar{f}(v) - \bar{f}(v_1))}\right)(\bar{f}(v) - \bar{f}(v_1))}{\left(1 + ae^{-\tau(\bar{f}(v_2) - \bar{f}(v_1))}\right)(\bar{f}(v_2) - \bar{f}(v_1))}(x_2 - x_1) \quad (4.5)$$

The fact that the hysteresis trajectory starting from a turning point targets all the previously recorded internal turning points enables the prediction of the response utilizing the proposed mapping strategy. Figure 4.4(b) depicts a typical hysteresis path originating from point (v_0, x_0) . If the input keeps increasing up to the maximum threshold point, the trajectory passes through all the internal target points $(v_1, x_1), (v_2, x_2), \dots, (v_{n-1}, x_{n-1})$ and approaches the upper threshold point (v_n, x_n) . The equation describing this path is given by:

$$x_{0n}(v) = \sum_{i=0}^{n-1} H(v, v_i, v_{i+1}) \times \left\{ x_i + \frac{\left(1 + ae^{-\tau(\bar{f}(v) - \bar{f}(v_i))}\right)(\bar{f}(v) - \bar{f}(v_i))}{\left(1 + ae^{-\tau(\bar{f}(v_{i+1}) - \bar{f}(v_i))}\right)(\bar{f}(v_{i+1}) - \bar{f}(v_i))}(x_{i+1} - x_i) \right\} \quad (4.6)$$

where $x_{0n}(v)$ denotes the predicted multi-segment hysteresis path, which will hold until the direction of input changes, and H represents the unit bilateral Heaviside function expressed as:

$$H(x, a, b) = \begin{cases} 1 & a \leq x \leq b \\ 0 & x > b \text{ or } x < a \end{cases} \quad (4.7)$$

By dividing the model into ascending and descending parts, identifying the average function parameters and mapping coefficients, assigning a memory organizer to record and wipe out the turning points, and initializing the memory units to the upper and lower threshold points, a model can be developed based on relationship (4.6) to predict any hysteresis response occur between the lower and the upper threshold points.

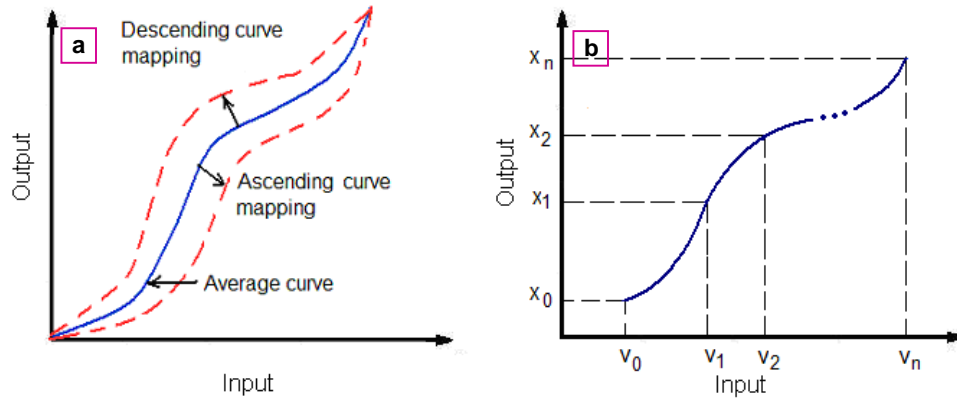


Figure 4.4 (a) Separation of nonlinearity from the hysteresis loops, and (b) typical multi-segment internal path.

4.4.2 Experimental Verification

A least square error minimization algorithm has been utilized here to identify parameters a and τ for the ascending and descending reference curves. Once these parameters are identified, they remain unchanged for the internal trajectories. This comes from the fact that all the internal hysteresis trajectories adopt their shape from the associated reference curves. The identified memory-based model is subjected to the same input profile given in Figure 4.2(a). The response

of the model is compared with the experimental data in Figure 4.5. As seen, the butterfly hysteresis loops have been precisely predicted through the proposed model. Furthermore, Figure 4.6 depicts the effectiveness of the model in predicting minor hysteresis loops. It is emphasized that to force the average curve to fit the ascending and descending reference curves only 4 parameters have been used (2 for ascending and 2 for descending curves). Adding the 10 coefficients of the average function, a total of 14 parameters are required to model the nonlinear behavior of a Galfenol micro-positioning actuator.

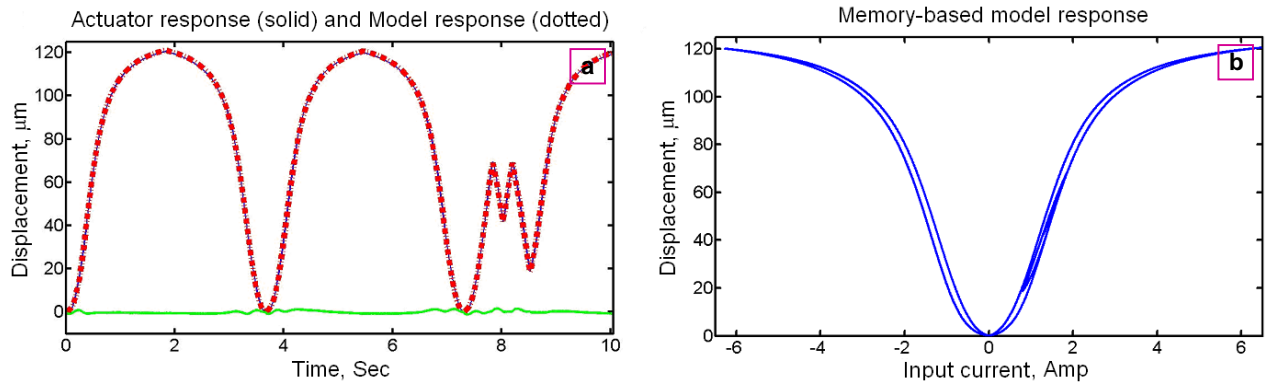


Figure 4.5 Performance of the memory based hysteresis model: (a) model vs. experimental time responses, and (b) model hysteresis response.

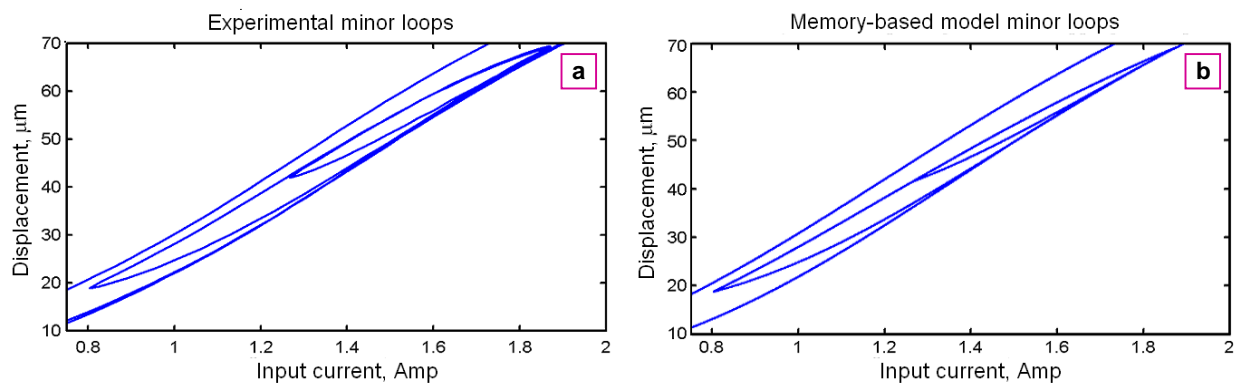


Figure 4.6 Minor hysteresis loops of (a) experimental and (b) memory-based model response.

To investigate the performance improvement of the proposed memory-based hysteresis framework over the average curve model, the error signals of both models are compared in Figure 4.7. Maximum error percentages and the average error values are presented in Table 4.1. The results indicate that around 400% improvement is achieved when the hysteresis prediction is added to the average curve model. For further demonstration of the actuator response to arbitrary input profiles, a numerical simulation is carried out as depicted in Figure 4.8. Results demonstrate the ability of the model in predicting multiple-loop hysteresis response for negative and positive values of input and for both left and right minor loops.

It is remarked that only rate-independent hysteresis loops can be modeled through this framework. To compensate for the effects of system frequency-dependent dynamics, appropriate models must be selected to account for the dynamical effects including system inertia and damping.

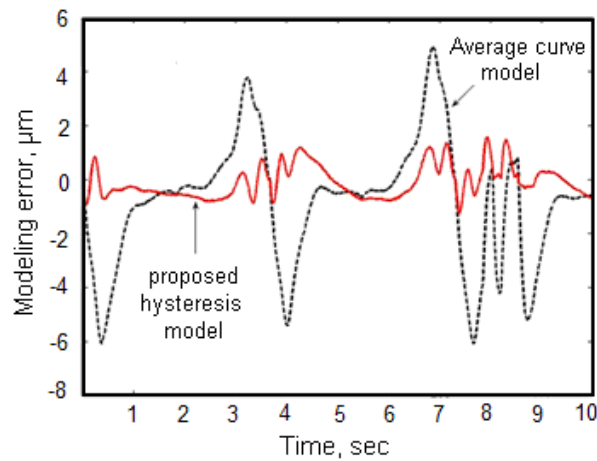


Figure 4.7 Error comparison of the average curve model and the memory-based hysteresis model.

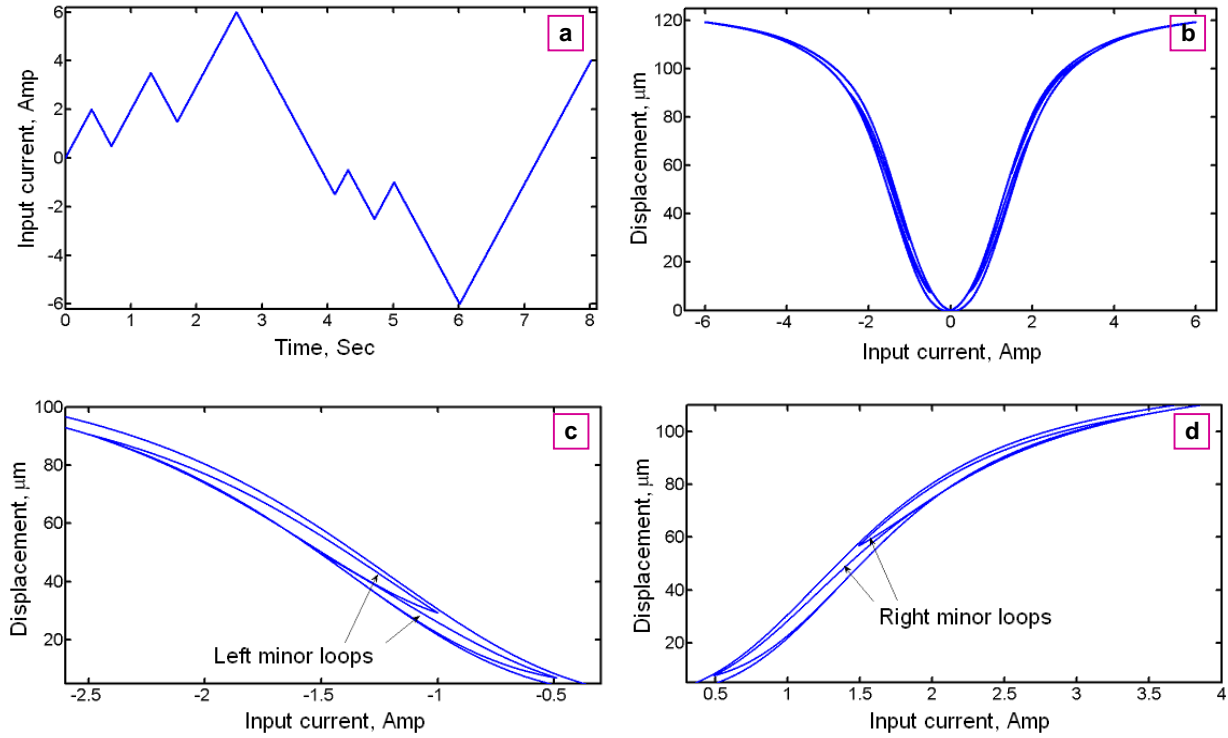


Figure 4.8 Simulation of hysteresis model: (a) input profile, (b) butterfly hysteresis response, (c) left minor loops, and (d) right minor loops.

Table 4.1 Comparison of the error values for the average curve model and the memory-based hysteresis model.

	Max. error	Avg. error
Average curve model	5.0232 %	1.7602 (μm)
Memory-based model	1.5431%	0.4364 (μm)

4.5 Proportional - Integral (PI) Hysteresis Control

The hysteresis nonlinearity in magnetostrictive actuators degrades its performance for the accurate positioning applications. Therefore, the hysteresis compensation is very essential while using smart actuators in micro-nano positioning.

The Proportional-Integral (PI) control is utilized in this section for controlling the nonlinear hysteresis behaviour of Galfenol micro positioning actuator. Figure 4.9 depicts the schematic of hysteresis compensation strategy using PI control. The hysteresis model developed in previous sections is used here for hysteresis compensation strategy development.

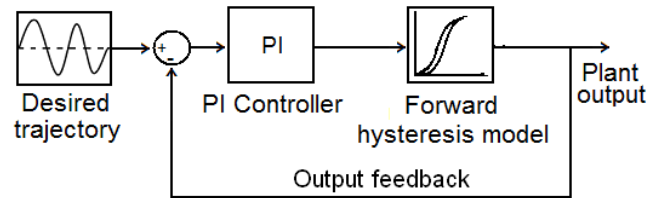


Figure 4.9 Hysteresis control using Proportional Integral control strategy

Numerical simulations for the hysteresis compensation for using PI controller are performed.

The tracking results for 500 and 1000Hz desired input frequencies are depicted in Figure 4.10.

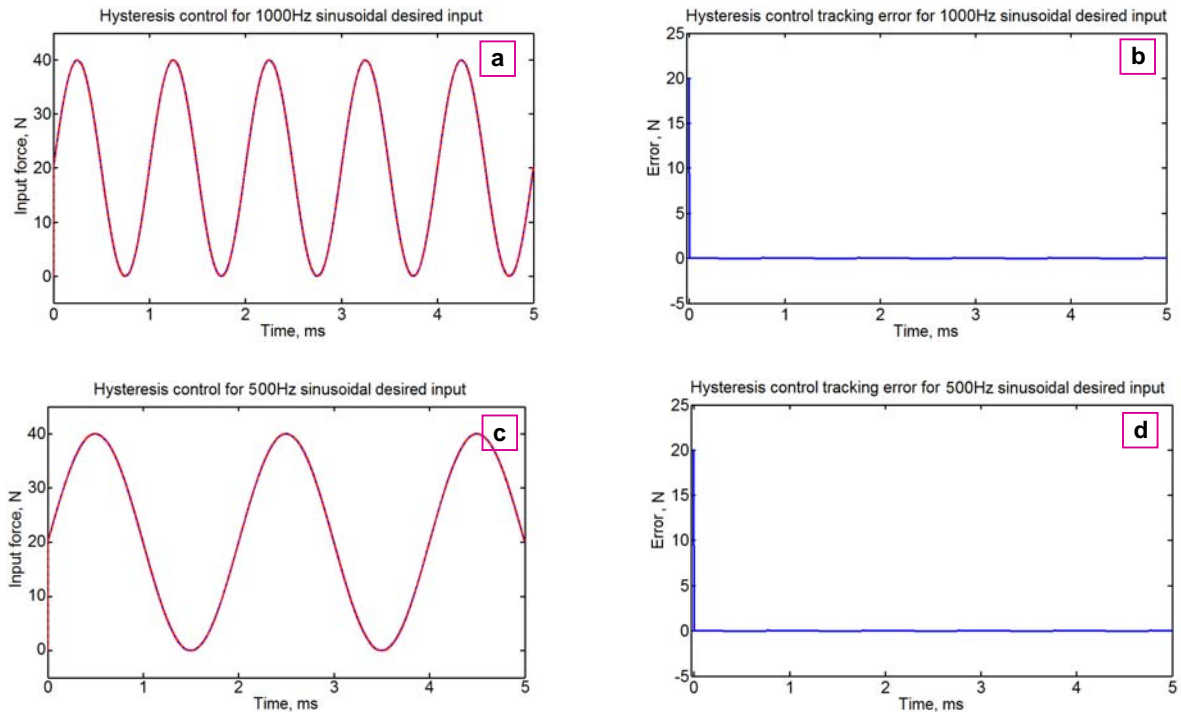


Figure 4.10 Hysteresis control results: (a) and (b) for 500Hz sinusoidal desired input, (c) and (d) for 1000Hz sinusoidal desired input

The proportional and integral gains, used in the numerical simulations are depicted in Table 4.2.

Table 4.2 Proportional and Integral gain values for 500 and 1000Hz sinusoidal desired input

Desired input frequency (Hz)	Proportional gain (k_p)	Integral gain (k_i)	Max. Error (N)
500	0.001	100,000	0.053
1000	0.001	50,000	0.05

After achieving the precise control of actuator dynamic behaviour and hysteresis nonlinearity independently, methods for combining them together are discussed in the next chapter. Also, further improvements in minor hysteresis loop prediction as well as hysteresis compensation technique are described in the future works.

CHAPTER 5

CONCLUSIONS AND FUTURE WORKS

5.1 Conclusion

The work presented here is focused on modeling and control framework of rod-like solid state Galfenol actuator. To achieve the simplicity in dynamic analysis and controller development, dynamic behavior of the actuator was modeled separately from the hysteresis nonlinearity. In order to get the insight of actuator dynamics, a distributed-parameters model of the actuator was developed. The free and the forced motion analyses were carried out to obtain the state-space representation of the actuator. Numerical simulations using different boundary mass and spring were carried out to emphasize their effect on the mode shapes and natural frequencies of the actuator.

A frequency based state space feedback controller utilizing Lyapunov theory was designed for achieving precise tracking control over the actuator motion. A full order state observer was developed to predict the states of the unobservable plant. A least square optimization method was used to obtain the optimal observer gain matrix. A robust, variable structure control was incorporated into the controller design to overcome the effects of plant structural uncertainties on tracking performance of the controller. Several numerical simulations were performed to observe the effect of modes deficiency on tracking frequency bandwidth of the controller.

In order to predict the nonlinear multi-loop hysteresis effect in the Galfenol actuator, the hysteresis nonlinearity was decoupled from the looping effect and modeled using an average

function. A hysteresis predictive model, based on intelligent hysteresis properties named as *targeting of turning points, curve alignment* and the *wiping-out effect* was developed utilizing a memory-based nonlinear mapping technique. The obtained average function was utilized in the hysteresis model for the accurate prediction of major as well as minor hysteresis loops. Numerical simulations for the hysteresis prediction were carried out using Matlab/Simulink model. A total of 14 parameters, 10 for average curve prediction and 4 more for forcing the average curve to accurately fit the ascending and descending hysteresis loops, were used in the model. Finally, a Proportional-Integral (PI) control strategy was used for the accurate hysteresis compensation. The tracking simulations for 500 and 1000Hz desired frequency input were carried out to validate the performance of the PI controller.

5.2 Future Works and Directions

In the work presented here, the problem of controlling the rod-like solid state Galfenol actuator is divided into two parts: The first half of the thesis describes the modeling and control of the actuator dynamics behavior while the second half deals with modeling and control of hysteresis nonlinearity. The combined control scheme that can control the actuator dynamic behaviour together with the hysteresis nonlinearity can be developed as future work. The schematic of the combined actuator dynamics and hysteresis control strategy using developed robust variable structure control and PI control is depicted in Figure 4.11.

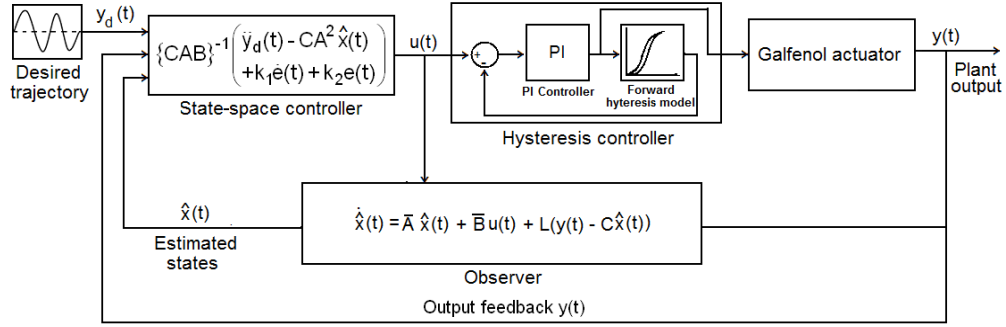


Figure 5.1 Combined hysteresis and actuator dynamics control scheme using combination of state-space and PI controller

As depicted in Figure 4.11, for combined dynamic and hysteresis control of the actuator, the output of the state-space feedback controller is fed as an input to the PI controller and output of the PI controller is applied as a controlled input to the plant.

In order to improve the accuracy in prediction of minor hysteresis loops, a mechanism can be incorporated into the hysteresis predictive model such that the shape of the minor hysteresis loops can be changed by varying few parameters in the hysteresis predictive model. Also, instead of using the PI control, an inverse hysteresis model utilizing the similar mapping technique as forward model can be developed for compensation of hysteresis. The schematic of combined actuator dynamics and hysteresis control is depicted in Figure 4.12. Instead of applying the output of state-space controller to PI controller, it is applied to the inverse hysteresis model and the output of the inverse hysteresis model is then applied to the plant as depicted in Figure 4.12.

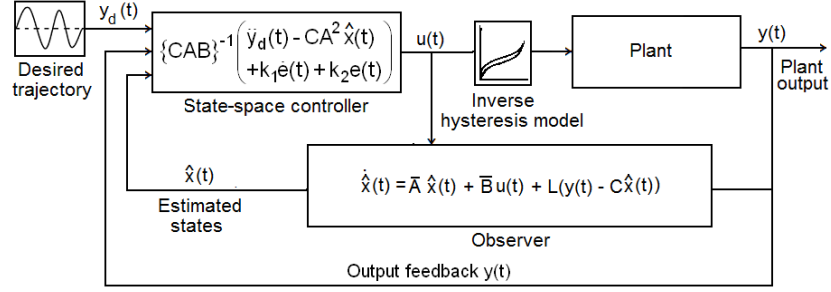


Figure 5.2 Combined hysteresis and actuator dynamics control scheme using combination of state-space and inverse hysteresis controllers

The hysteresis prediction results using inverse hysteresis model with 14 mathematical parameters 10 average curve parameters and 4 shaping parameters are depicted in Figure 4.13. The accuracy of inverse hysteresis prediction can be significantly increased by increasing the number of mathematical parameters in the inverse model used for the inverse hysteresis prediction in the model.

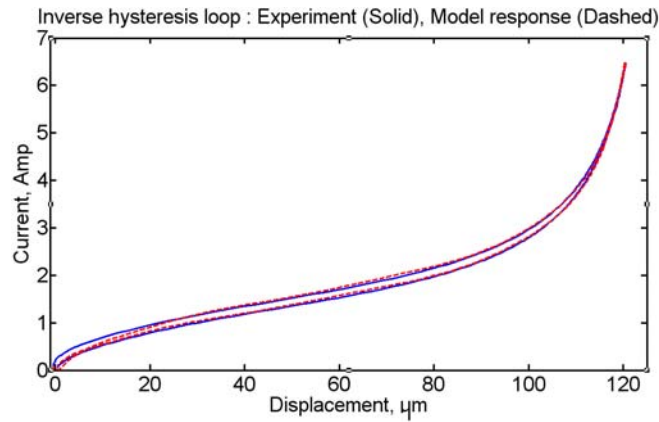


Figure 5.3 Hysteresis prediction using inverse hysteresis model

The modeling and control framework presented in this work can be implemented on most of the rod-like solid-state smart actuators. The proposed control strategy for the smart actuators will widen their usage for the precision-positioning applications.

APPENDIX

Derivation of Orthogonality Conditions for Mode Shape Functions

In order to obtain the orthogonality condition, the separation of variable is applied to undamped free boundary condition of actuator as:

$$m\phi_r(L)\ddot{q}_r(t) + EA\phi_r'(L)q_r(t) + k\phi_r(L)q_r(t) = 0 \quad (\text{A.1})$$

Substituting Eq. (2.13) into Eq. (1) and rearranging the required terms, Eq. (1) yields:

$$\phi_r'(L) = \frac{\gamma\phi_r(L)}{EA} \quad (\text{A.2})$$

where

$$\gamma_r = (m\omega_r^2 - k) \quad (\text{A.3})$$

The equation of motion in the spatial domain for r^{th} and s^{th} mode of the actuator can be represented as:

$$\phi_r''(x) = -\beta_r^2\phi_r(x) \quad (\text{A.4})$$

and

$$\phi_s''(x) = -\beta_s^2\phi_s(x) \quad (\text{A.5})$$

Multiplying Eq. (A.4) by $\phi_s(x)$ and Eq. (A.5) by $\phi_r(x)$, integrating over the actuator length and taking integral by parts, they can be rewritten as:

$$\phi_r'(L)\phi_s(L) - \int_0^L \phi_r'(x)\phi_s'(x)dx = -\beta_r^2 \int_0^L \phi_r(x)\phi_s(x)dx \quad (\text{A.6})$$

$$\phi_s'(L)\phi_r(L) - \int_0^L \phi_s'(x)\phi_r'(x)dx = -\beta_s^2 \int_0^L \phi_s(x)\phi_r(x)dx \quad (\text{A.7})$$

Subtracting Eq. (A.7) from Eq. (A.6) and using Eq. (A.2), one can obtain:

$$(\beta_r^2 - \beta_s^2) \left\{ \rho \int_0^L \phi_r(x)\phi_s(x)dx + m\phi_r(L)\phi_s(L) \right\} = 0 \quad (\text{A.8})$$

For the two distinct r^{th} and s^{th} modes, i.e., $\omega_r \neq \omega_s$, Eq. (A.8) can be restated as:

$$\rho \int_0^L \phi_r(x) \phi_s(x) dx + m \phi_r(L) \phi_s(L) = 0 \quad (\text{A.9})$$

when $\omega_r = \omega_s$.

Hence we have:

$$\rho \int_0^L \phi_r(x) \phi_s(x) dx + m \phi_r(L) \phi_s(L) \neq 0 \quad (\text{A.10})$$

Integrating (A.9) and (A.10) and applying the normalization condition for the mode shapes, yields:

$$\rho \int_0^L \phi_r(x) \phi_s(x) dx + m \phi_r(L) \phi_s(L) = \delta_{rs} \quad (\text{A.11})$$

Eq. (A.11) represents the orthogonality condition for the longitudinal vibrations of the actuator with respect to mass. In order to obtain the orthogonality condition with respect to stiffness, we substitute Eq. (A.2) into Eq. (A.6), and rearrange the required terms to get:

$$EA \int_0^L \phi_r'(x) \phi_s'(x) dx + k \phi_r(L) \phi_s(L) = \omega_r^2 \delta_{rs} \quad (\text{A.12})$$

Eq. (A.12) represents the orthogonality condition with respect to stiffness.

REFERENCES

- [1] http://en.wikipedia.org/wiki/Smart_materials
- [2] <http://www.answers.com/topic/smart-material?cat=technology>
- [3] Chen, Hong, “Smart nanotechnology in biomaterials, sensors, actuators and textiles”, *Proceedings of AIChE Annual Meeting and Fall Showcase*, pp. 3382-3383 , Oct. 2005, Cincinnati, OH, United States.
- [4] Pan C. T., Shiea J. and Shen S.C., “Fabrication of an integrated piezo-electric micro-nebulizer for biochemical sample analysis” *Journal of micromechanics and microengineering*, **17**, pp. 659–669, February 2007.
- [5] Sater J.M., Lesieutre G., Martin C., “ A smarter transition for smart technologies [aerospace engineering]” *Aerospace America*, **44**, pp.18-21, June 2006.
- [6] Martin A. C., Hallam B. J., Flanagan J. S., Bartley J., “Design, Fabrication, and Testing of a Scaled Wind Tunnel Model for the Smart Wing Project” *Journal of Intelligent Material Systems and structures*, **15**, pp. 269-78, April 2004
- [7] Koh J. H., Jeong S. J., Ha M. S., Song J.S. “Aging of piezoelectric properties in $\text{Pb}(\text{MgNb})\text{O}_3 - \text{Pb}(\text{ZrTi})\text{O}_3$ multilayer ceramic actuators” *Journal of applied physics*, **96**, pp.544-8, July 2004
- [8] Zickgraf B., Schneider G.A., Aldinger F., “Fatigue behavior of multilayer piezoelectric actuators” Max-Planck-Institut für Metallforschung Pulvermetallurgisches Laboratorium Heisenbergstraße 5, 70569 Stuttgart, Germany
- [9] <http://www.etrema-usa.com/core/terfenold/>
- [10] Kellogg R. A., Russell A. M., Lograsso T. A., Flatau A. B., Clark A. E. and Wun-Fogle M., "Tensile properties of magnetostrictive iron-gallium alloys," *Acta Materialia*, **52**, pp.5043- 5050, 2004.

- [11] Wun-Fogle M., Restorff J. B., Clark A. E., Dreyer E. and Summers E., "Stress annealing of Fe–Ga transduction alloys for operation under tension and compression," *Journal of Applied Physics*, **97**, pp. 10M301-1-3, 2005.
- [12] Wun-Fogle M., Restorff J. B. and Clark A. E., "Magnetomechanical coupling in stress-annealed Fe–Ga (Galfenol) alloys," *IEEE Transactions on Magnetics*, **42**(10), pp. 3120-2 2006.
- [13] Letty R. L., Claeysen F., Barillot F., And Lhermet N. A., "Amplified Piezoelectric Actuators for aerospace applications" *Workshop on Smart Materials and Structures* pp.51–62, September 2003.
- [14] Giessibl F. J., "Advances in atomic force microscopy", *Reviews of Modern Physics*, **75**, pp. 949-983, 2003.
- [15] Gonda S., Doi T., Kurosawa T., Tanimura Y., Hisata N., Yamagishi T., Fujimoto H., and Yukawa H., "Accurate topographic images using a measuring atomic force microscope," *Applied Surface Science*, **144–145**, pp. 505-509, 1999.
- [16] Vora K., Bashash S., and Jalili N., "Distributed parameters modeling of rod-like solid-state actuators," in *Proceeding of 1st ASME Dynamic Systems and Control Conference*, October 2008, Ann Arbor, MI.
- [17] Ping G., and Musa J., "Modeling hysteresis in piezoceramic actuators," *Precision Engineering*, **17**, pp. 211-221, 1995.
- [18] Kuhnen K., and Janocha H., "Inverse feedforward controller for complex hysteretic nonlinearities in smart-material systems," *Control and Intelligent Systems*, **29**, pp. 74-83, 2001.
- [19] Ang W. T., Garmon F. A., and Khosla P. K., Riviere C. N., "Modeling rate-dependent hysteresis in piezoelectric actuators," *Proceeding of IEEE International Conference on Intelligent Robots and Systems*, **2**, pp. 1975-1980, Oct. 2003.

- [20] Bashash S., and Jalili, N., “Robust multiple-frequency trajectory tracking control of piezoelectrically-driven micro/nano-positioning systems”, *IEEE Transactions on Control Systems Technology*, **15** (5), pp. 867-878, 2007.
- [21] Tzen J. J., Jeng S. L., and Chieng W. H., “Modeling of piezoelectric actuator for compensation and controller design,” *Precision Engineering*, **27**, pp. 70-76, 2003.
- [22] Aderiaens H., Koning W., and Banning R., “Modeling piezoelectric actuators,” *IEEE/ASME Transactions on Mechatronics*, **5**, pp. 331-341, 2000.
- [23] Smith R., “Smart material systems: Model developments”, SIAM, Philadelphia, PA, 2005
- [24] Aderiaens H., Koning W. and Banning R. “Modeling piezoelectric actuators” *IEEE/ASME Trans. Mechatronics* **5**, pp.331–41, 2000
- [25] Goldfarb M. and Celanovic N., “A lumped parameter electromechanical model for describing the nonlinear behavior of piezoelectric actuators” *ASME J. Dyn. Syst. Meas. Control* **119**, pp.478–85, 1997
- [26] Krasnosel’skii M. A. and Pokrovskii A. V., “Systems with Hysteresis” (Berlin: Springer), 1989
- [27] Visintin A. “Differential Models of Hysteresis ” (Berlin: Springer), 1994
- [28] Bashash S. and Jalili N., “Intelligence rules of hysteresis in the feedforward trajectory control of piezoelectrically-driven nanostagers”, *Journal of micromechanics and microengineering*, **17**, pp. 342-9, December 2006
- [29] Preisach F., “Über die magnetische nachwirkung” (in German),. *Zeitschrift für physik*, **94**, pp. 277, 1935.

- [30] Bashash S. and Jalili N., "A New Constitutive Modeling and Control Paradigm for Piezoelectrically-actuated Nanostagers", *ASME International Mechanical Engineering Congress and Exposition*, pp. 10p, November 2006, Chicago, Illinois, USA
- [31] Lining S., "Tracking control of piezoelectric actuator based on a new mathematical model", *J. Micromech. Microeng.* **14**, pp.1439–44 , 2004
- [32] Ang W. T., Garmon F. A., Khosla P. K. and Riviere C. N., "Modeling rate-dependent hysteresis in piezoelectric actuators", *Proc. IEEE Int. Conf. Intel. Robots and Syst. (Las Vegas, NV, 27–31 October)* **2**, pp.1975–80, 2003
- [33] Ping Ge, Jouaneh M., "Tracking control of a piezoceramic actuator", *Proceeding of IEEE Transactions on Control Systems Technology*, **4**, pp. 209-16, May 1996
- [34] Zhong J., Yao B., "Adaptive robust precision motion control of a piezoelectric positioning stage" *Proceeding of IEEE Transactions on Control Systems Technology*, **16**, pp.1039-1046, Sept. 2008
- [35] Sasaki M., Kawafuku M., Takahashi K., "Comparison of feedback controllers for feedback-error-learning neural network control system with application to a flexible micro-actuator" *IEEE International Conference on Systems, Man, and Cybernetics. Computational Cybernetics and Simulation (Cat.No.97CH36088-5)*, **5**, pp.4035-40 1997